RESEARCH ARTICLE

Aged and *BRCA*-Mutated Stromal Cells Drive Epithelial Cell Transformation

Geyon L. Garcia[1], Taylor Orellana[2], Grace Gorecki[3], Leonard Frisbie[4], Roja Baruwal[5], Swathi Suresh[3], Ester Goldfeld[1], Ian Beddows[6], Ian P. MacFawn[7], Ananya K. Britt[1], Macy M. Hale[3], Amal Taher Elhaw[3,8], Brian R. Isett[7], Nadine Hempel[3], Riyue Bao[7], Hui Shen[6], Ronald J. Buckanovich[3,9], Toren Finkel[10], Ronny Drapkin[11], T. Rinda Soong[12], Tullia C. Bruno[7], Huda I. Atiya[3], and Lan G. Coffman[2,3,9]

ABSTRACT The fundamental steps in high-grade serous ovarian cancer (HGSOC) initiation are unclear, presenting critical barriers to the prevention and early detection of this deadly disease. Current models propose that fallopian tube epithelial (FTE) cells transform into serous tubal intraepithelial carcinoma (STIC) precursor lesions and subsequently into HGSOC. In this study, we report that an epigenetically altered mesenchymal stem cell niche, termed high-risk mesenchymal stromal/stem cell (hrMSC), exists prior to STIC lesion formation. hrMSCs are enriched in STIC stroma and contribute to a stromal "field effect" extending beyond the borders of the STIC lesion. hrMSCs promote DNA damage in FTE cells while also fostering FTE cell survival. hrMSCs induce malignant transformation of the FTE, resulting in metastatic cancer *in vivo*, indicating that hrMSCs promote cancer initiation. hrMSCs are significantly enriched in *BRCA1/2* mutation carriers and increase with age. Combined, these findings indicate that hrMSCs can incite ovarian cancer initiation and have important implications for ovarian cancer detection and prevention.

SIGNIFICANCE: This work demonstrates a critical role of fallopian tube stromal cells in HGSOC initiation with implications for the pathophysiology of HGSOC formation and the development of prevention and early detection strategies critically needed in this disease. Additionally, the identification of stromal-mediated epithelial transformation has broad implications for understanding pan-cancer initiation.

See related commentary by Recouvreux and Orsulic, p. 1093

INTRODUCTION

Ovarian cancer is the most lethal gynecologic cancer, with more than 13,000 U.S. women dying yearly (1). High-grade serous ovarian carcinoma (HGSOC) is the most common ovarian cancer subtype, with more than 70% of patients presenting with metastatic disease at the time of diagnosis (2). This is attributed to multiple factors, including a nonspecific and gradually worsening symptom burden and a lack of effective screening or early detection strategies. There is a critical need to identify and understand the mechanisms of HGSOC initiation, which can then be leveraged to derive effective prevention and early diagnosis approaches.

Due to the inability to screen for ovarian cancer, the current approach to primary prevention is surgical castration with bilateral salpingo-oophorectomies in women with *BRCA1* or *BRCA2* germline mutations. *BRCA1* and *BRCA2* mutations are well-characterized risk factors conveying a roughly 39% to 58% and 13% to 29% lifetime risk of developing HGSOC, respectively (2). However, the majority of HGSOC tumors develop in the absence of germline *BRCA1* or *BRCA2* mutations, suggesting that malignant transformation is achieved by other, currently undefined mechanisms. Convincing evidence has demonstrated that the majority of HGSOC tumors arise from the fallopian tube epithelium (FTE), with the immediate precursor lesion of HGSOC termed a serous tubal intraepithelial carcinoma (STIC; refs. 3–6). STIC lesions are a series of *TP53*-mutated epithelial cells demonstrating atypical morphology and an increased proliferative index indicative of increased malignant behavior (7–9). Research on STIC lesions has mainly focused on changes within epithelial cells, whereas the microenvironment surrounding STIC lesions has largely been unexplored. Evidence from other cancer types demonstrates that changes in the stromal microenvironment may create a permissive or even causative environment that promotes cancer initiation (10–12). It is clear that the microenvironment plays a critical role in the pathophysiology of HGSOC; however, the role of the fallopian tube microenvironment in HGSOC initiation is undefined and thus presents a critical gap in our current understanding of this disease.

[1]University of Pittsburgh School of Medicine, Pittsburgh, Pennsylvania. [2]Division of Gynecologic Oncology, Department of Obstetrics, Gynecology, and Reproductive Sciences, University of Pittsburgh School of Medicine, Pittsburgh, Pennsylvania. [3]Division of Malignant Hematology & Medical Oncology, Department of Medicine, UPMC Hillman Cancer Center, University of Pittsburgh School of Medicine, Pittsburgh, Pennsylvania. [4]Integrative Systems Biology, University of Pittsburgh, Pittsburgh, Pennsylvania. [5]Department of Pharmacology & Chemical Biology, University of Pittsburgh, Pittsburgh, Pennsylvania. [6]Center for Epigenetics, Van Andel Research Institute, Grand Rapids, Michigan. [7]Department of Immunology, University of Pittsburgh School of Medicine, Pittsburgh, Pennsylvania. [8]Department of Pharmacology, College of Medicine, Pennsylvania State University, Hershey, Pennsylvania. [9]Magee Women's Research Institute, University of Pittsburgh School of Medicine, Pittsburgh, Pennsylvania. [10]Aging institute, University of Pittsburgh, Pittsburgh, Pennsylvania. [11]Department of Obstetrics and Gynecology, Penn Ovarian Cancer Research Center, Basser Center for BRCA, Abramson Cancer Center, University of Pennsylvania Perelman School of Medicine, Philadelphia, Pennsylvania. [12]Department of Pathology, University of Pittsburgh, Pittsburgh, Pennsylvania.

G.L. Garcia and T. Orellana are co-first authors of this article.

H.I. Atiya and L.G. Coffman are co-senior authors of this article.

Corresponding Author: Lan G. Coffman, University of Pittsburgh Medical Center, The Assembly Building, 5051 Centre Avenue, Pittsburgh, PA 15213. E-mail: coffmanl@upmc.edu

Cancer Discov 2025;15:1203–24

doi: 10.1158/2159-8290.CD-24-0805

Our group previously demonstrated that mesenchymal stromal/stem cells (MSC), a multipotent stromal progenitor cell found in most adult tissues, can be reprogrammed by cancer cells to form cancer-associated mesenchymal stem cells (CA-MSC; ref. 13). These HGSOC-educated CA-MSCs exhibit a tumor-supportive phenotype that enhances tumor cell growth, confers chemoresistance, enriches the cancer stem-like cell pool, promotes angiogenesis, and aids in the metastatic spread of HGSOC tumor cells (13–16). The protumorigenic phenotype of CA-MSCs is accompanied by a unique DNA methylation, RNA expression, and protein expression profile that differs from nontumorigenic or normal MSCs (nMSC). Using these data, we discovered that CA-MSCs rely on the expression of the transcription factor Wilms tumor protein 1 (WT1) to carry out their protumorigenic function (13).

In this study, using a cohort of primary patient samples, we identified a subset of fallopian tube–derived MSCs from women without cancer that phenocopy cancer-educated CA-MSCs. This group of MSCs exhibited similar epigenetic and transcriptomic changes to CA-MSCs, including high expression of WT1. This subset of MSCs is enriched in women with *BRCA1* or *BRCA2* mutations, increases with age, and is found within the stroma surrounding STIC lesions, creating a stromal "field effect" that extends well beyond the borders of the transformed epithelium. Spatial transcriptomic analysis confirms that stromal changes are correlated with the distance from the STIC lesion, providing independent evidence of a stromal field effect, which precedes malignant epithelial transformation. Additionally, MSCs exhibit a tumor-supportive phenotype like their cancer-associated counterparts. That is, these MSCs, which we refer to as high-risk MSCs (hrMSC), enhance tumor cell growth, chemoresistance, and sphere formation and increase the proliferation and "stemness" of FTE cells. Most notably, hrMSCs trigger full malignant transformation of primary, noncancerous FTE cells *in vivo*, thus indicating that hrMSCs are mediators of HGSOC initiation. In support of these findings, we demonstrate that hrMSCs are potent inducers of DNA damage in FTE and promote the recovery of FTE following oxidative stress: two mechanisms that are linked to HGSOC initiation. This work describes the tumor-initiating function of hrMSCs and begins to elucidate an important mechanism of HGSOC formation, highlighting the critical role of the stroma in oncogenesis.

RESULTS

hrMSCs Are Present in the Microenvironment of STIC Lesions

Our previous work demonstrated that cancer-educated CA-MSCs are present in virtually all invasive HGSOC cases (13). However, the timing of CA-MSC development remained unclear. Therefore, we first asked whether similar stromal cells are found surrounding preinvasive STIC lesions. We previously demonstrated that the high expression of WT1 can distinguish CA-MSCs from nMSCs (13). Thus, to visualize and quantify CA-MSC–like cells in the STIC microenvironment, a multispectral Vectra imaging panel was developed to identify WT1-positive MSCs in patient tissues. All tissue samples were verified for histopathologic features of normal versus STIC-containing versus invasive HGSOC-containing fallopian tubes by clinical diagnosis and secondarily verified by an independent board-certified gynecologic pathologist (T.R. Soong and R. Drapkin; Fig. 1A). Cross sections of invasive HGSOC were used as positive controls (Supplementary Fig. S1A). STIC lesions fulfilled pathologic criteria of >10 contiguous cells with nuclear atypia, increased proliferative index (>10% Ki67$^+$), and *TP53* mutation IHC pattern (abnormal increased staining or null pattern). Representative STIC lesion, hematoxylin and eosin (H&E), and p53 IHC are presented in Supplementary Fig. S1. Tissues were analyzed for CA-MSC localization and abundance by Vectra multispectral imaging (Fig. 1A–F). A representative, multiplexed, stitched cross section is shown for reference (Supplementary Fig. S1B). MSCs were identified in the stroma by coexpression of the classic MSC surface markers CD73, CD90, and CD105. We further distinguished CA-MSC–like cells from nMSCs by WT1 expression (CD45$^-$/CD73$^+$/CD90$^+$/CD105$^+$/WT1$^+$). Given the lack of invasive carcinoma in our STIC samples, we herein refer to the CA-MSC–like cells (WT1$^+$ MSCs) as hrMSCs. Intriguingly, we observed hrMSCs within the stroma adjacent to and underlying STIC lesions (Fig. 1A; red x), whereas hrMSCs were rarely detected in normal patient fallopian tubes.

To further assess hrMSC spatial distribution and quantify the number of hrMSCs within the fallopian tube surrounding STIC lesions, we selected patient samples with STIC lesions that were incidental ($n = 6$) and STIC lesions with concurrent invasive disease ($n = 11$) and compared these with patient samples with invasive HGSOC within the fallopian tube ($n = 4$) or completely normal fallopian tubes ($n = 2$). We sought to determine if there was a stromal "field effect," with hrMSCs involving stroma that extended beyond the boundaries of the STIC lesion. We thus quantified the abundance of hrMSCs and nMSCs directly underlying the STIC lesions as well as the stroma underlying FTE contiguous to the STIC region (the first 20 normal, monolayered epithelial cells directly contiguous to the STIC lesion on both sides), the stroma underlying FTE adjacent to the STIC region (within 2 mm of the STIC lesion on both sides), and the stroma underlying distal FTE (>2 cm away from STIC lesions; Fig. 1B–D). We compared these groups with hrMSCs found in normal fallopian tubes and CA-MSCs found within the invasive HGSOC microenvironment. Given that most STICs occur in the distal fimbriated end of the fallopian tube (FT), we limited our investigation to this portion of the fallopian tube. Raw cell numbers (hrMSC or nMSC) were quantified and normalized by the tissue area analyzed and presented as hrMSC and nMSC abundance and hrMSC/nMSC ratio (Fig. 1B–D).

Importantly, hrMSCs were significantly enriched in the stroma directly underlying STIC epithelium (Fig. 1C). This was equivalent to CA-MSC abundance in invasive carcinoma. hrMSC abundance was also increased in contiguous and adjacent areas but decreased to significantly lower levels in the stroma distal to STIC epithelium. nMSC abundance remained consistent across groups but was decreased in the stroma of invasive carcinoma. The ratio of hrMSC to nMSC was significantly higher in STIC-associated stroma and remained high in the contiguous and adjacent regions with a decrease in the regions distal to the STIC lesions. However, even in the distal regions, both the total number of hrMSCs and the ratio of hrMSC to nMSC remained higher than in

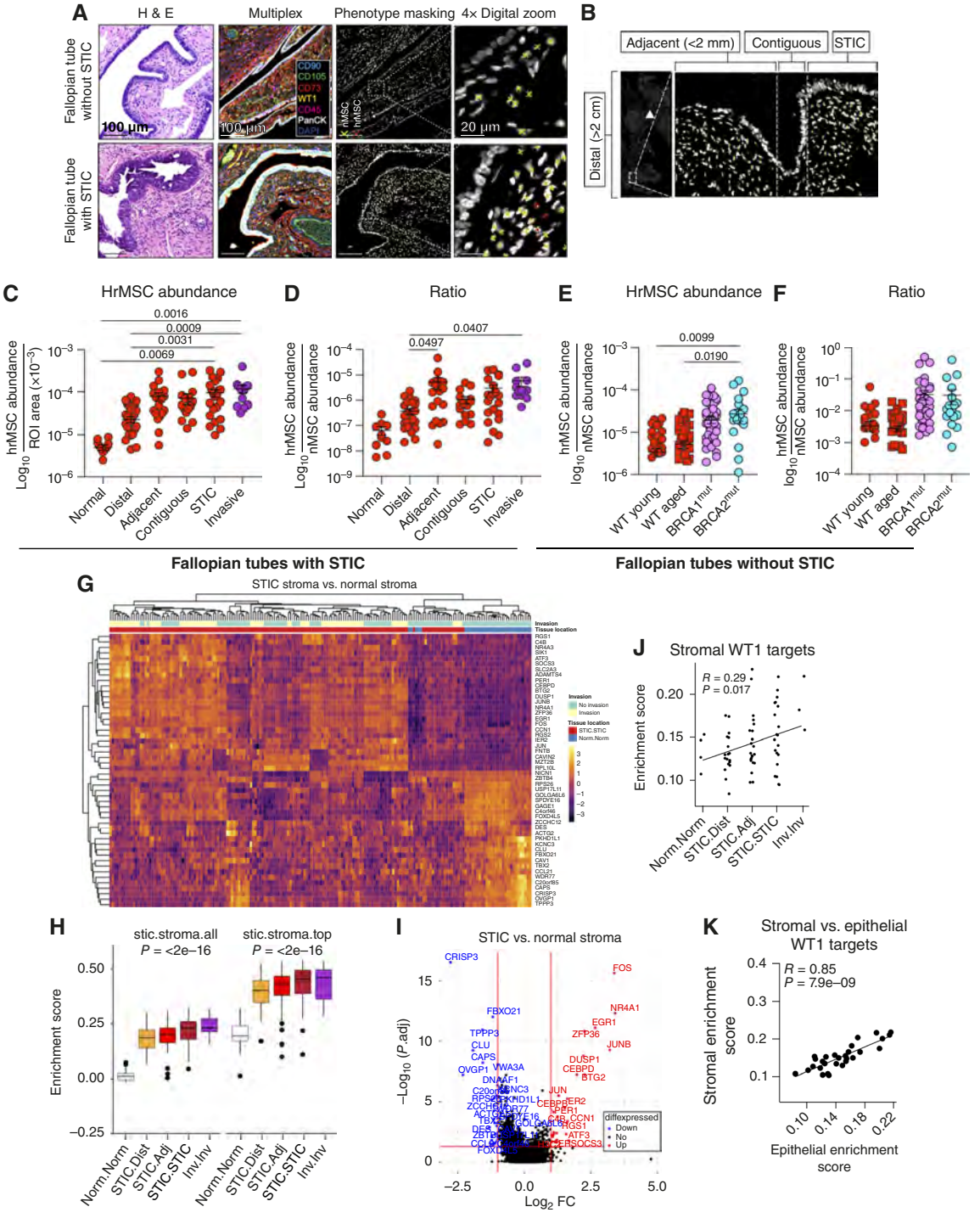

Figure 1. hrMSCs are enriched in the stroma underlying and adjacent to fallopian tube STIC lesions. **A,** Representative H&E-stained tissue sections of normal fallopian tubes and fallopian tubes harboring STIC lesions. Histology is paired with multispectral IF images of each respective group shown. Black and white images denote cells with the phenotypes of interest. Red x's indicate hrMSCs (WT1$^+$/CD73$^+$/CD90$^+$/CD105$^+$/CD45$^-$), whereas yellow x's indicate nMSCs (WT1$^-$/CD73$^+$/CD90$^+$/CD105$^+$/CD45$^-$). **B,** Schematic showing the criteria for the Vectra spatial quantification. **C,** hrMSC abundance normalized to the area of ROI. **D,** hrMSC to nMSC ratios. **E,** hrMSC abundance (normalized to the area of ROI) in the expanded normal FT patient cohorts consisting of WT ($n = 10$ young, $n = 9$ aged), *BRCA1* mutant ($n = 9$), or *BRCA2* mutant ($n = 6$) fallopian tubes lacking STIC/HGSOC. **F,** Ratio of hrMSC/nMSC in normal FTs. *P* values were determined by ordinary one-way ANOVA with Tukey's multiple comparisons analysis. Data points for **C**–**F** are reflective of individual ROIs. Statistics were determined on field ROIs for **C** and **D**. Statistics were determined with patient averages for **E** and **F**. **G,** Heatmap with unsupervised clustering of STIC stroma vs. normal stroma. **H,** Enrichment score of DEGs between STIC stroma vs. normal stroma (left: all, right: top 30 genes) applied to stromal location [from normal to STIC distal (dist) to STIC adjacent that contains both STIC contiguous and adjacent regions (STIC adj) to directly underlying STIC to invasive stroma]. **I,** Volcano plot of significantly differentially expressed genes in STIC stroma vs. normal stroma. **J,** Enrichment score of WT1 targets in stroma applied to stromal locations as in **I**. **K,** Correlation of stromal WT1 enrichment score with epithelial WT1 enrichment score.

normal fallopian tubes (though this did not reach statistical significance; Fig. 1D). Interestingly, the abundance of hrMSCs found surrounding incidental STIC lesions (STIC lesions without associated invasive cancer) and STIC lesions with concurrent invasive cancer identified elsewhere was not statistically different (Supplementary Fig. S1C).

We also demonstrated that hrMSCs are present in the fallopian tubes of women without STIC lesions (completely histologically normal tubes). The initial two normal fallopian tubes analyzed were from women with a germline *BRCA1* mutation. Given the 30- to 40-fold increased risk of developing HGSOC in patients with germline *BRCA1* or *BRCA2* mutations (*BRCA1*^{mut} *or BRCA2*^{mut}), we hypothesized that hrMSCs are enriched in the fallopian tubes of germline mutation carrier patients, which may account for some of the increased risk of developing HGSOC. We obtained additional normal fallopian tubes (without any identifiable precancerous lesions or other pathology) from *BRCA1*^{mut} carriers ($n = 9$), *BRCA2*^{mut} carriers ($n = 6$), and patients without *BRCA1/2* mutations/wild-type (WT) patients (*BRCA1/2*^{wt}; $n = 19$). Representative images used for quantification are shown in Supplementary Fig. S1D. Given the increased risk of HGSOC with age, we divided the *BRCA*^{wt} patients into two age groups: 30 to 36 years old and 60 to 72 years old. The prevalence of hrMSCs was significantly higher in the *BRCA2*^{mut} carriers, with a trend toward increased prevalence in the *BRCA1*^{mut} carriers compared with *BRCA1/2*^{wt} patients (Fig. 1E and F). There was also a trend toward increased hrMSC prevalence in the older *BRCA1/2*^{wt} patients compared with the younger patients (Fig. 1E), but this did not reach statistical significance. Statistical differences were based on individual patient averages shown in Supplementary Fig. S1E. nMSC abundance from STIC to distal stroma (Fig. 1F; Supplementary Fig. S1F) and in aged and *BRCA1*/2 mutant patients (Supplementary Fig. S1G) is shown as a reference.

To further understand the stromal differences in STIC lesions versus normal fallopian tube stroma and expand upon the concept of a stromal field effect, we used serial sections from the patients in our initial Vectra cohort and added an additional five STIC samples, two invasive samples, and two normal samples (total $n = 22$ STIC, $n = 6$ invasive, $n = 4$ normal) and performed GeoMx digital spatial profiling (DSP). We again divided regions of the fallopian tube based on the location pertaining to the STIC (underlying STIC, contiguous, adjacent, and distal) and compared this with regions of completely normal fallopian tubes and fallopian tubes with invasive HGSOC (Fig. 1G–K). Tissue was segmented into epithelial compartments or stromal compartments (excluding CD45$^+$ immune cells), and the transcriptomic profile was assessed for each region and each cell type. Epithelial heatmaps are shown in Supplementary Fig. S1H. We demonstrate clear differences in the stroma underlying STIC lesions compared with normal fallopian tube stroma [Fig. 1G and I, full differentially expressed genes (DEG) list in Supplementary Table S1]. Interestingly, when the differential gene set of STIC stroma versus normal stroma (referred to as the STIC stromal signature) is applied to stromal locations surrounding the STIC, there is a distinct pattern related to location (Fig. 1H). Of note, the contiguous and adjacent regions were combined because of limited cell numbers in the "contiguous" location and the strong similarities in the transcriptional profile in these two groups. The STIC stromal signature remains pronounced in locations surrounding the STIC lesion but becomes less prominent with increasing distance from the STIC. Averaged stromal gene enrichments for all stromal genes and top stromal-enriched genes further underscore the unique transcriptional profile of STIC stroma (Supplementary Fig. S1I). However, even in regions distal from the STIC, there remains enrichment for the STIC stromal signature, arguing that stromal changes persist even at locations far removed from the premalignant lesion. Similarly, the STIC stromal signature is most pronounced in the invasive HGSOC stroma. This indicates that changes in the stroma surrounding STIC lesions reflect changes that occur in the stroma of fully invasive HGSOC (Fig. 1H). Collectively, these data support the formation of a stromal field effect within fallopian tubes bearing STIC lesions. Interestingly, this field effect is marked by an increasing WT1 transcriptomic signature, in line with the findings of an increased presence of WT1$^+$ hrMSCs (Fig. 1J). This indicates that hrMSCs may be drivers of the stromal field effect. When examining the epithelial compartment, as expected, there are clear transcriptomic differences in the STIC epithelium versus normal epithelium (Supplementary Fig. S1H and S1J). When comparing stroma with its overlying epithelium, there was a strong correlation between stromal WT1 enrichment and epithelial WT1 enrichment (Supplementary Fig. S1K). As high WT1 expression is a marker of HGSOC, this supports a cross-talk between the two cellular compartments, further supporting an important role for stromal influences on the epithelium during HGSOC initiation (Fig. 1K). Representative H&E and p53 IHC of STIC lesions used for DSP analysis are presented in Supplementary Fig. S1L.

hrMSCs Have the Epigenomic and Transcriptomic Pattern of Tumor-Supportive CA-MSCs

We previously demonstrated that CA-MSCs have unique DNA methylation profiles that distinguish them from nMSCs (13, 16). Therefore, we utilized the Infinium Methylation EPIC array to compare the DNA methylation pattern of MSCs from normal fallopian tubes of women with *BRCA1/2*^{mut} to MSCs isolated from *BRCA1/2*^{wt} normal fallopian tube, ovary, or omental tissue or CA-MSCs isolated from invasive HGSOC (involving the fallopian tube, ovary, or omentum; Fig. 2A; ref. 13). As mentioned previously, patient fallopian tubes were analyzed by sectioning and extensively examining the fimbriated end (SEE-FIM) protocols to validate the absence of STIC or invasive cancer (17). Uniform Manifold Approximation and Projection for Dimension Reduction (UMAP) and unsupervised hierarchical clustering revealed that roughly half of *BRCA1/2*^{mut} fallopian tubes contained MSCs (red circles) that clustered with CA-MSCs (purple circles), whereas the rest of *BRCA1/2*^{mut} MSCs clustered with nMSCs (Fig. 2B). A single patient was removed from this analysis to eliminate neoadjuvant treatment as a confounding factor in our analysis (Supplementary Fig. S2A). When assessing the patient characteristics of these samples, the average age of patients whose tubes contained hrMSCs was 47.5 years compared with 45 years in those that did not. There was no difference in race, menopausal status, or parity between patients with and without hrMSCs. Interestingly, 75% of the tubes that contained hrMSCs were from *BRCA2*^{mut} carriers, whereas 75% of tubes with only nMSCs

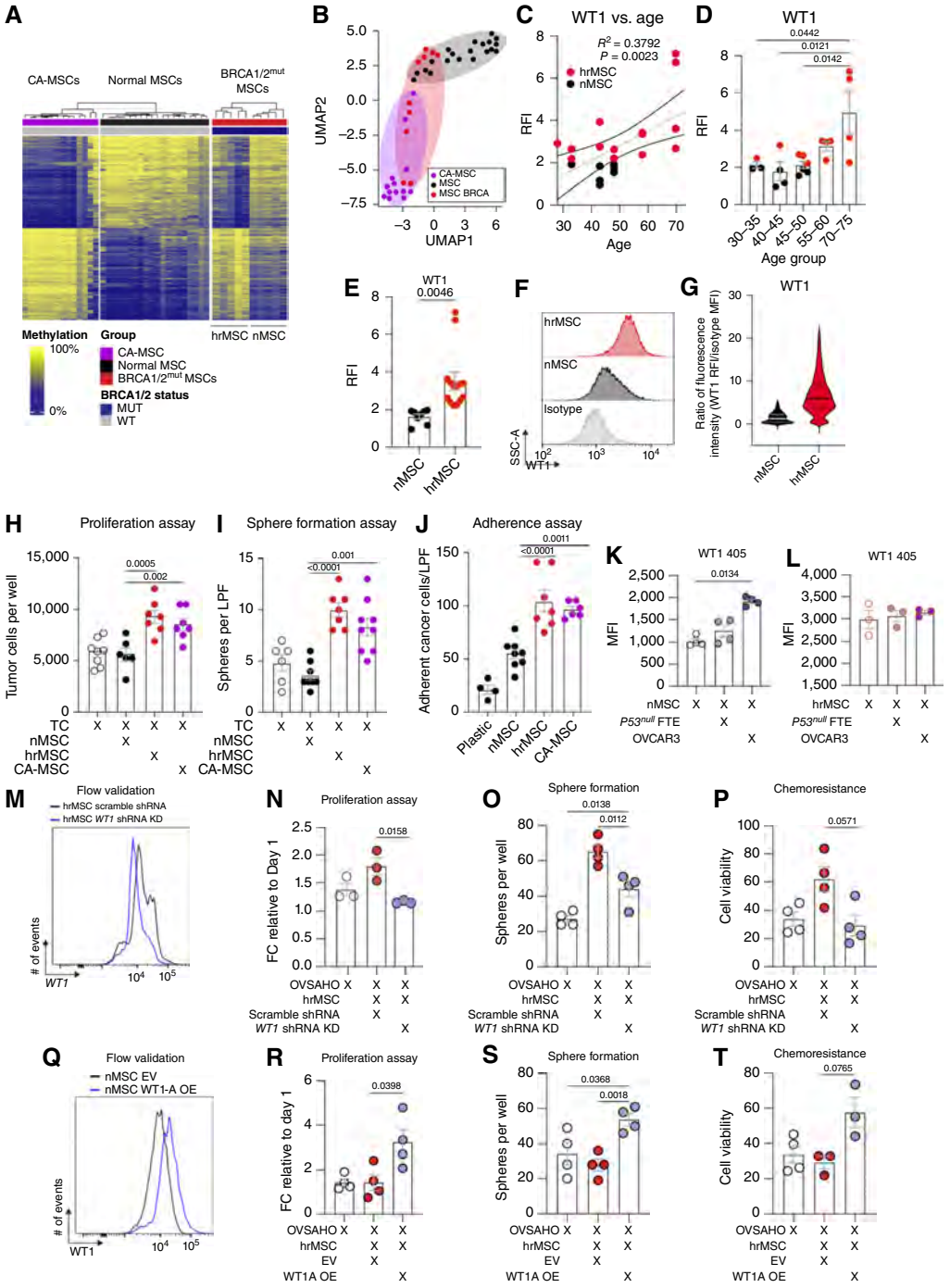

Figure 2. hrMSCs exhibit the epigenetic and phenotypic profile of CA-MSCs. **A,** DNA methylation array represented as a heatmap. MSCs were taken from benign patient tissues (nMSCs; black circles; $n = 20$), *BRCA1/2*^{mut} carrier patients without cancer (red circles; $n = 10$), and patients with confirmed invasive HGSOC (CA-MSC; purple circles; $n = 14$). **B,** UMAP of MSCs derived from patients in **A**. **C,** Relative fluorescence intensity (RFI) of WT1 405 was determined by flow cytometry for WT ($n = 5$), *BRCA1*^{mut} ($n = 3$), and *BRCA2*^{mut} ($n = 13$) MSC cell lines. WT1 405 RFI was plotted against patient age. Linear regression of WT1 405 MFI vs. patient age (gray line); $R^2 = 0.3745$. **D,** MSCs were categorized into age groups. **E,** MSCs were classified into nMSCs or hrMSCs based on WT1 405 RFI with a minimum cutoff of 2 RFI for hrMSCs. This categorization was independent of *BRCA* status and age. **F** and **G,** Representative histograms and violin plots of nMSC and hrMSC WT1 expression. **H** and **I,** Ovarian tumor cells (TC) were grown independently or in coculture with nMSCs, hrMSCs, or CA-MSCs under adherent (**H**) or nonadherent (**I**) conditions. Individual cells and spheroids per low powered field (LPF) were counted and graphed ($n = 3$). **J,** Tumor cell adherence to nMSCs, hrMSCs, and CA-MSCs is shown ($n = 3$). For **D–J**, *P* values were determined by ordinary one-way ANOVA with Tukey's multiple comparison analysis. **K** and **L,** WT1 MFI determined by flow cytometry following coculture of nMSCs or hrMSCs in monoculture or coculture with FTE or ovarian cancer cells. **M,** *WT1* KD and scramble shRNA control hrMSCs were generated by lentiviral transduction and validated by flow cytometry. **N–P,** Relative fold change (FC) of tumor cells after coculture with *WT1* shRNA KD or scramble shRNA hrMSCs under (**N**) adherent or (**O**) nonadherent conditions. **P,** Chemoresistance assay on the aforementioned cocultures. **Q–T,** Similarly, *WT1* OE or empty vector (EV) nMSCs were generated using lentiviral transduction. Tumor cells were cocultured with transduced lines, and tumor cell proliferation, sphere formation, and chemoresistance were assessed.

were from *BRCA1*^{mut} carriers. These data are in line with our Vectra imaging data demonstrating the presence of hrMSCs in some fallopian tubes of women with *BRCA1/2* mutations, even in the absence of STIC or invasive cancer (Fig. 1).

Given that the expression of WT1 is critical to CA-MSC development and can distinguish tumor-supportive CA-MSCs from nMSCs (13), we next quantified WT1 protein expression across an independent, expanded additional set of normal fallopian–derived MSCs (from either *BRCA1/2*^{wt} or *BRCA1/2*^{mut}) via flow cytometry (Fig. 2C–G). We used WT1 expression from CA-MSCs to set a threshold. All CA-MSC cells express WT1 at ≥2 relative fluorescence intensity, whereas nMSCs decrease below 2 relative fluorescence intensity; therefore, we used this threshold to define a fallopian tube MSC as an hrMSC or nMSC (Fig. 2E; Supplementary Fig. S2B). WT1 expression significantly increased with patient age, and significantly more hrMSCs were present in the fallopian tubes of older women (Fig. 2C and D; $R^2 = 0.3792$). In this expanded sample set, the average age of women with hrMSCs was 10 years older than those with nMSCs (53 vs. 43 years old). In some cases, WT1 expression varied between contralateral tubes of the same patient. It is important to note that MSCs derived from a patient were not uniformly WT1 high or WT1 low; rather, these populations existed on a spectrum indicating a mixed population or a population with evolving WT1 expression (Fig. 2F and G). These data are consistent with our multispectral imaging data above, demonstrating that hrMSCs are enriched in aged fallopian tubes and can be distinguished from nMSCs by WT1 expression. For the remainder of Fig. 2, we sought to determine whether hrMSCs possess tumor-supportive functions similar to CA-MSCs (Fig. 2H–J); whether precancerous epithelial changes promote WT1 expression, thus facilitating tumor support (Fig. 2K and L); and whether WT1 expression was driving the overall tumor-supportive phenotype (Fig. 2M–T). To determine if hrMSCs arise from precancerous changes in overlying FTE, we performed coculture experiments with nMSCs and noncancerous FTE that harbor a *TP53* mutation (*P53*^{null}), given that the *TP53* mutation is one of the earliest events in HGSOC initiation. *P53*^{null} FTE coculture led to a slight, nonsignificant increase in nMSC WT1 levels that did not reach hrMSC thresholds. As a control, fully transformed HGSOC tumor cells significantly increased WT1 expression in nMSCs to hrMSC thresholds consistent with our prior work demonstrating that HGSOC converts nMSCs into CA-MSCs. Interestingly, hrMSCs that already express high levels of WT1 show no change after exposure to *p53*^{null} FTE or HGSOC tumor cells (Fig. 2K and L).

hrMSCs Enhance Cancer Cell Growth, Sphere Formation, and Adherence to Ovarian Tumor Cells

To determine if hrMSCs are phenotypically like their CA-MSC counterparts and have tumor-supportive functions, we tested the impact of hrMSCs on critical aspects of HGSOC biology. When possible, assays were performed using matched hrMSCs and nMSCs (hrMSCs and nMSCs derived from contralateral fallopian tubes from the same woman to control for patient heterogeneity). CellTrace Violet (CTV)–labeled HGSOC cells (OVCAR3, OVSAHO, and primary patient line 412) were grown with hrMSCs, nMSCs, or primary HGSOC-derived CA-MSCs at a 1:1 ratio to assess the impact of hrMSCs on HGSOC proliferation. The percentage of viable cells relative to day 0 was counted at 3 time points (representative time course shown in Supplementary Fig. S2C). hrMSCs increased the proliferation of HGSOC cells 2-fold compared with nMSCs (Fig. 2H), which was equivalent to the proliferation enhancement demonstrated by CA-MSC controls. A critical function of CA-MSCs is their ability to directly bind cancer cells and form heterocellular complexes under nonadherent conditions (13). We performed sphere assays to test the impact of hrMSCs on cancer cell growth under nonadherent conditions. The number of cancer cell–containing spheres was equivalent between hrMSC and CA-MSC coculture groups, whereas nMSCs failed to enhance sphere formation (Fig. 2I). We also compared the ability of hrMSCs to directly adhere to cancer cells with plastic and Poly-D-Lysine (PDL) used as negative and positive controls, respectively (Supplementary Fig. S2D). Cancer cells bound to hrMSCs at a level equivalent to CA-MSCs (~2- to 3-fold higher than nMSCs; Fig. 2J). These data demonstrate that hrMSCs are functionally equivalent to HGSOC-derived CA-MSCs in their support of ovarian cancer cell proliferation, sphere formation, and adherence to cancer cells. To determine if WT1 mediates the tumor-supportive function of hrMSCs, we generated *WT1* short hairpin RNA (shRNA) knockdown (KD) and *WT1* overexpressing (OE) cells with m-GFP lentiviral transduction. Transduced MSCs, validated using flow cytometry (Fig. 2M and Q), were sorted on m-GFP and cocultured with tumor cell lines (OVSAHO, OVCAR3) for 5 days. *WT1* KD hrMSCs demonstrated a significant reduction in hrMSC-mediated tumor cell growth, sphere formation, and chemoresistance (Fig. 2N–P). Additionally, *WT1* OE nMSCs resulted in increased MSC-mediated tumor cell growth, sphere formation, and chemoresistance, indicating that WT1 expression mediates the tumor-supportive function of hrMSCs (Fig. 2R–T).

hrMSC Tumor-supportive Functions Give Rise to Increased Proliferation and Increased DNA Damage in FTE

Given the presence of hrMSCs within normal aging and *BRCA1/2*^{mut} FTs and their abundance surrounding STIC lesions, we hypothesized that hrMSCs play a role in FTE transformation and HGSOC initiation. We first characterized the effects of hrMSCs on FTE cell growth and sphere formation under direct coculture conditions. Primary patient-derived, germline *BRCA1/2*^{mut} carrier FTE or immortalized FTE (FT190 control) cells were labeled with CTV and cocultured with hrMSCs or nMSCs. By day 4, hrMSCs and nMSCs both significantly increased the proliferation of FTE cells compared with FTE grown alone (Fig. 3A). When cocultured under nonadherent conditions, however, only hrMSCs significantly increased the growth of FTE spheroids, whereas nMSCs did not (Fig. 3B). CA-MSCs also enrich the stem-like population of tumor cells *in vitro* (13). We therefore tested the ability of hrMSCs to affect the stemness of FTE cells. FTE cells that were cocultured with hrMSCs demonstrated significantly increased aldehyde dehydrogenase (ALDH) activity, a marker of "stemness," compared with FTE cells cultured alone or in coculture with

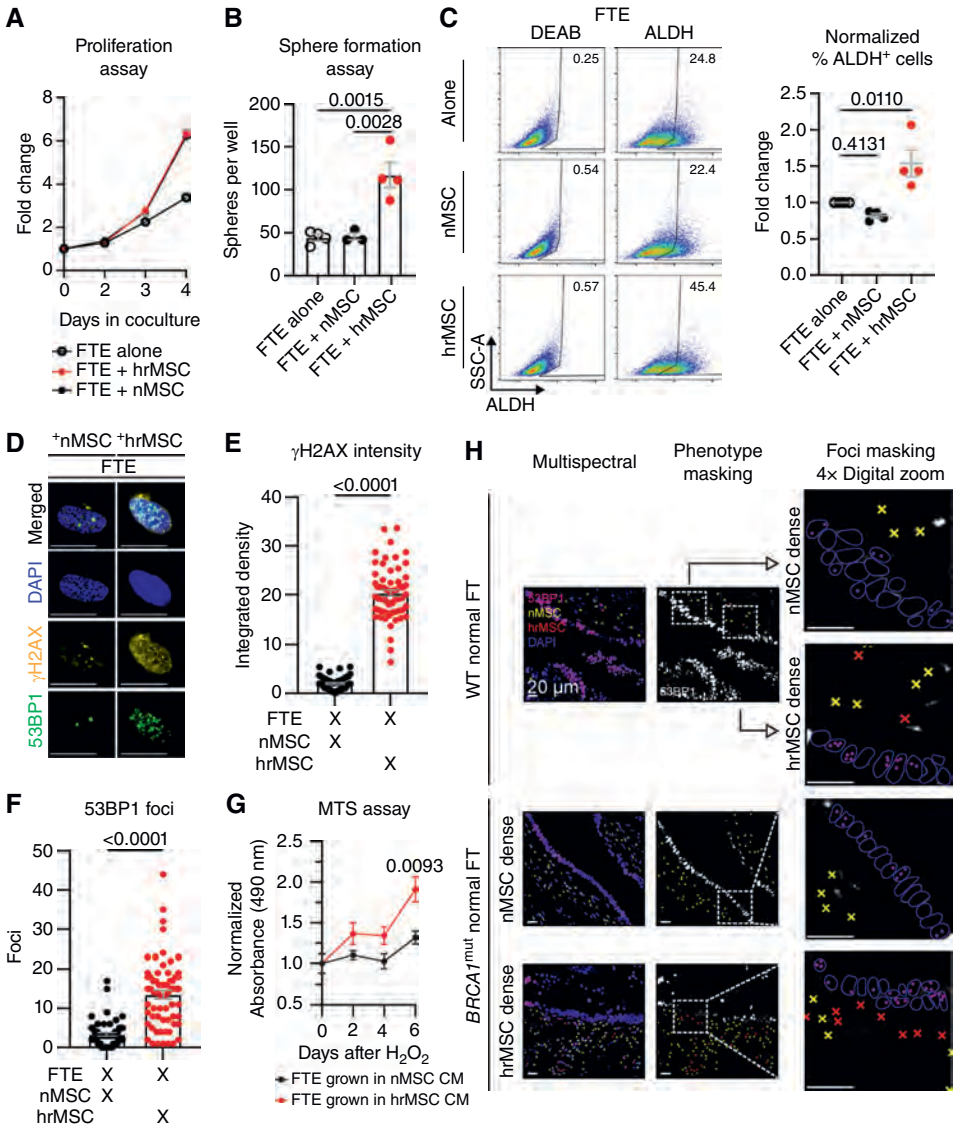

Figure 3. hrMSCs increase FTE proliferation and stemness, induce DNA damage in FTE, and enhance the recovery of FTE following oxidative stress. **A,** Primary FTE were grown in coculture with matched nMSCs, hrMSCs, or alone for up to 4 days. Each day, the total number of viable cells was determined ($n = 3$). **B,** Primary FTE were grown under nonadherent conditions with or without nMSCs and hrMSCs. Spheroids were grown for 7 days and manually counted ($n = 3$). **C,** The percentage of ALDH$^+$ primary FTE cells or FT190 control cells was determined by flow cytometry after 5 days of adherent coculture with or without nMSCs or hrMSCs. The percentage of total cells that are ALDH$^+$ is shown as well as representative flow plots ($n = 3$). Primary FTE and immortalized FT190 control cells were cocultured for 24 hours alone or with nMSCs or hrMSCs. **D–F,** Representative IF images of FTE cells (**D**), γH2AX fluorescence intensity (**F**) and 53BP1 foci per nucleus by fluorescent microscopy ($n > 3$) (**F**). Individual data points reflect individual nuclei. **G,** Primary FTE and FT190 control cells were treated with 50 μmol/L hydrogen peroxide for 10 minutes in FBS-free media and supplemented with either nMSC conditioned media (CM) or hrMSC CM. **G,** Cell viability was determined by MTS assay ($n > 3$). **H,** Representative multispectral images of FTE with DNA DSBs (53BP1 foci) overlying either nMSC dense or hrMSC dense stroma in WT or *BRCA1*^{mut} fallopian tubes. For **A**–**G**, *P* values were determined by *t* test or two-way ANOVA with Tukey's multiple comparison analysis.

nMSCs (Fig. 3C). These data indicate that hrMSCs also support growth and potential stemness in nontransformed epithelial cells.

DNA damage, DNA double-strand breaks (DSB), and DNA repair defects are well-known hallmarks of HGSOC; therefore, we next assessed the impact of hrMSCs on FTE DNA damage and recovery (Fig. 3D–G). We assayed FTE cells for generalized DNA damage with γH2AX and DSBs by 53BP1 foci. Like hrMSCs (Supplementary Fig. S3A–S3C), cocultured FTE cells exhibited robust DNA damage and DNA DSBs (Fig. 3D–F). Importantly, we validated this finding in primary patient samples *in situ*. We applied our hrMSC Vectra multispectral imaging panel and incorporated staining for 53BP1 foci in normal *BRCA1/2*^{wt} and *BRCA1*^{mut} fallopian tubes (without STIC; representative phenotype masked and multiplexed images are shown in Supplementary Fig. S3D and S3E). We observed that, in areas with a high prevalence of hrMSCs, the associated FTE demonstrated a higher relative abundance of 53BP1 foci compared with FTE in nMSC-enriched regions (Fig. 3H).

The high burden of DNA DSBs in FTE cells exposed to hrMSCs led us to question whether hrMSCs confer a survival and/or recovery advantage to FTE cells following DNA damage. To test this, we treated FTE cells with a DNA damaging agent (50 μmol/L hydrogen peroxide). This dose is the minimum effective dose used to elicit cell death in FTE cells. Following treatment, we neutralized the peroxide and supplemented FTE cells with conditioned media from nMSCs or hrMSCs every other day for 6 days, and viable FTE cells were quantified over time. Indeed, hrMSC conditioned media promotes increased cell recovery following peroxide treatment relative to nMSC controls (Fig. 3G). Thus, in addition to promoting FTE cell growth and stemness, hrMSCs also induce DNA DSBs and, at the same time, support FTE survival under stress, suggesting the ability to recover following DNA damage.

hrMSCs Induce Full Malignant Transformation

Given the striking impact of hrMSCs on FTE DNA damage, recovery, and proliferation, we next tested the impact of hrMSCs on FTE malignant transformation. We first created organoids from primary patient-derived, benign FTE cells with (i) *TP53*-null mutation (*P53*^{null} FTE) or (ii) germline heterozygous *BRCA1*^{mut} FTE or *BRCA2*^{mut} FTE with hrMSCs or nMSC in a 1:1 FTE/MSC ratio. FTE-alone or MSC-alone organoids were also created as controls. Organoids developed within 7 days and were maintained in culture for 4 to 10 weeks. Representative *P53*^{null} FTE + nMSC or hrMSC organoids are shown in Supplementary Fig. S4A. Organoids were then dissociated to ensure efficient injection and prevent mechanical shearing. Single-cell suspensions were normalized based on epithelial cell number—1×10^5 FTE per injection—and injected into the mammary fat pad of NOD/SCID gamma (NSG) mice. Organoids containing *P53*^{null} FTE or *BRCA1*^{mut} FTE alone failed to initiate tumors. Organoids with hrMSCs alone or nMSCs alone also did not initiate tumors. Similarly, organoids containing *P53*^{null} FTE or *BRCA1*^{mut} FTE grown with nMSCs did not initiate tumors over 12 months. In total, *P53*^{null} FTE + hrMSC organoids (5 of 14) and *BRCA1*^{mut} FTE + hrMSCs (2 of 10) initiated tumors within 4 months (Fig. 4A–C). Three of the five *P53*^{null} + hrMSC organoids that initiated tumors also developed metastatic disease to the lung and liver. Representative images of a primary and metastatic tumor are shown (Fig. 4B). WT FTE (FTE without *TP53*, *BRCA*, or any other known mutation) organoids were difficult to sustain; thus, only two mice per group were injected with WT FTE/MSCs after 4 weeks of organoid growth. Interestingly, one of two WT FTE/hrMSC organoids initiated tumors, whereas none of the WT FTE/nMSC organoids initiated tumors (Fig. 4A).

We next assessed functional changes in transformed FTE that initiated tumors. *P53*^{null} FTE were isolated from primary tumors and lung lesions 6 months after the injection of *P53*^{null} FTE/hrMSC organoids. Human cells were enriched from the xenografts using mouse cell depletion kits. Residual human MSCs or differentiated human stroma were removed with FACS sorting on the EPCAM$^+$, CD73/90/105-cell population. The isolated transformed *P53*^{null} FTE were propagated *ex vivo* and plated for proliferation and chemoresistance assays. Compared with the original primary *P53*^{null} FTE, the transformed *P53*^{null} FTE demonstrated a significantly higher proliferation rate and increased resistance to cisplatin treatment (Fig. 4D and E). Additionally, the transformed *P53*^{null} FTE demonstrated immortalization without replicative senescence. Compared with the parent *P53*^{null} FTE line, in which cells underwent senescence after 8 to 12 passages, the transformed *P53*^{null} FTE have been passaged over 80 times with a doubling time of ~24 hours. To further confirm full malignant transformation, we performed a secondary initiation experiment using an orthotopic model. The transformed *P53*^{null} FTE, after *ex vivo* propagation, were injected into the ovarian bursa of NSG mice and allowed to grow for 3 months. To quantify the time to engraftment, a subset of the transformed *P53*^{null} FTE were transduced with luciferase lentivirus to enable tracking with *in vivo* imaging system (IVIS) imaging. In this subset of tumors, engraftment was seen by week 2 with evidence of metastasis by week 7 after injection (Fig. 4F and G). All other mice bearing transformed *P53*^{null} FTE (without luciferase to prevent any confounding of results from viral transfection) were sacrificed at 3 months to assess tumor initiation and burden. All mice (12 of 12) demonstrated tumor engraftment with local invasion. Five of twelve mice demonstrated lung and liver metastasis. Tumors were excised and validated with histopathology by our gynecologic pathologist (T.R. Soong), demonstrating high-grade carcinoma morphology, epithelial origin (Supplementary Fig. S4B), and loss of p53 expression (consistent with the parent FTE line harboring a *TP53* null mutation; Fig. 4H). Collectively, these data demonstrate stromal-mediated FTE cell transformation.

Transformed FTE Cells Exhibit Genomic HGSOC Mutation Signatures

HGSOCs bear hallmark mutation signatures, and certain mutation signatures can infer potential mechanisms of DNA damage (7, 18–20). Thus, to characterize the genomic alterations in the transformed FTE and shed light on the underlying DNA damage mechanism in our model, we conducted whole-genome sequencing on our transformed, metastatic *P53*^{null} FTE cell lines. Compared with the nontransformed parental FTE cell line, transformed FTE cells acquired increased somatic mutations broadly (Supplementary Fig. S5A and S5B) and in genes associated with HGSOC, namely *BRCA1* and *APC*, as well as structural variants (Fig. 5A and B). Moreover, we performed single-base signature analysis on our whole-genome sequencing data and compared this with COSMIC mutational signatures. Interestingly, we discovered that each sample exhibited single-base mutational signatures 1, 2, and 5, with signature 5 having the strongest relative frequency (Fig. 5C; signature 5 for the other two metastatic samples is shown in Supplementary Fig. S5C). Double-base signatures were analyzed for each sample but were inconclusive (Supplementary Fig. S5D). Signature 5 has an unknown etiology; however, it has been associated with DNA damage resulting from replication stress, chronic exposure to reactive oxygen species (ROS), and aging. To determine if this correlated with our above DSP data (Fig. 1G–K; hrMSC enrichment in STIC stroma), we conducted gene set enrichment analysis on STIC stroma and normal stroma. Interestingly, WT1 pathway targets and oxidative stress signatures (e.g., oxidative stress-induced damage) were upregulated in STIC stroma compared with normal stroma (Fig. 5D). This is

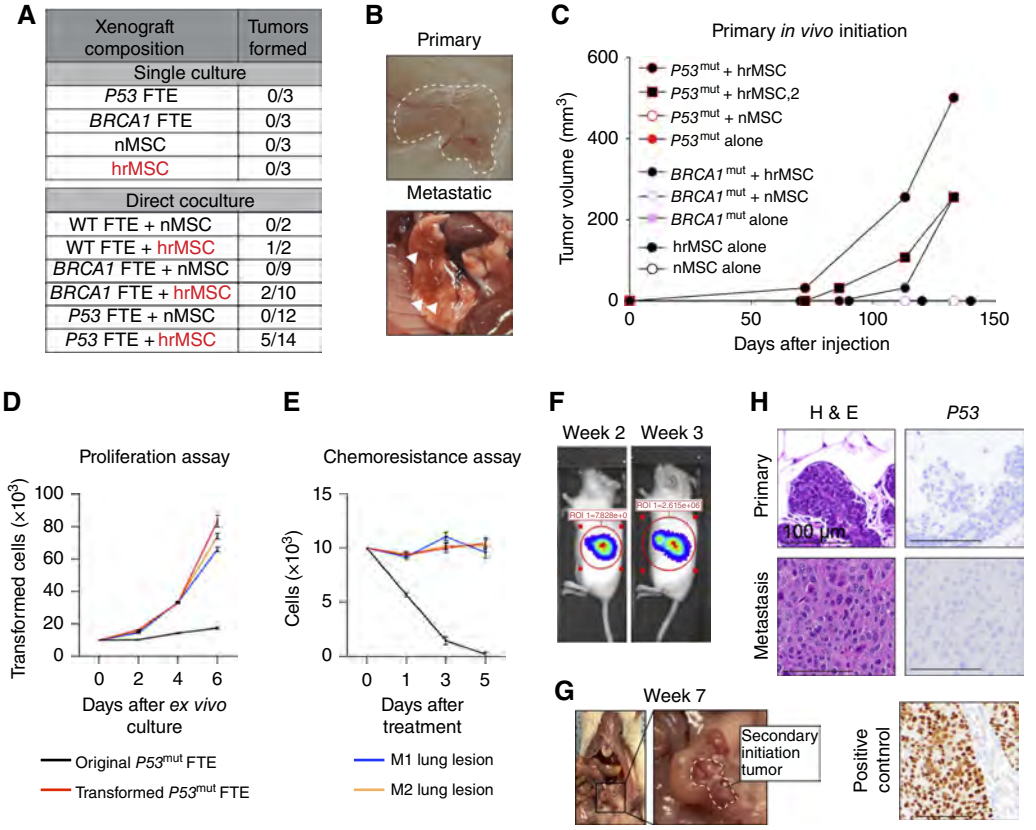

Figure 4. hrMSCs induce malignant transformation of primary FTE cells. Primary FTE cells were cultured under nonadherent conditions alone or with either nMSCs or hrMSCs. Cocultures were grown for 4–10 weeks and then injected into the fat pad of NSG mice. **A,** Total number of mice that developed tumors. **B,** Macroscopic representative images of primary tumors and secondary metastases. **C,** Tumor volume per mouse was graphed over the course of 5 months. **D,** Tumor cells from the primary and metastatic tumors were excised, dissociated, and passaged for up to 6 days *ex vivo*. **E,** Tumor cells were treated with 1 μg/mL cisplatin, and cell growth was determined up to 5 days ($n = 3$). In **D** and **E**, 12 wells per cell line per time point were analyzed, and statistics were determined by two-way ANOVA with Bonferroni correction. All three transformed lines compared with the primary epithelial line had a P value < 0.0001 in both panels. **F,** IVIS imaging of a representative mouse after weeks 2 and 3 of secondary initiation ($n = 1$). **G,** Gross anatomy of the tumor initiation site. Tumors were allowed to grow for 2 weeks before IVIS imaging began. **H,** Tumors were excised and processed for H&E and p53 IHC staining.

best exemplified in Fig. 5E, in which we observe enrichment of genes associated with oxidative stress–induced senescence in the stroma of STIC and invasive lesions. We analyzed STIC and normal FTE signatures and observed similar signatures; specifically, there was enrichment in oxidative stress and DNA damage pathways, further suggesting a potential link between hrMSC oxidative stress and the acquisition of epithelial mutations (Fig. 5F).

Next, we sought to validate this *ex vivo* by comparing levels of oxidative stress between patient-derived MSC cell lines using the general ROS probe CellROX. Compared with nMSCs, hrMSCs exhibited increased CellROX green fluorescence via immunofluorescence (IF) (Fig. 5G) and increased CellROX Deep Red (DR) fluorescence via flow cytometry (Fig. 5H; the gating scheme is shown in Supplementary Fig. S5E). hrMSC oxidative stress was reduced to nMSC levels with a single 24-hour treatment of the antioxidant Trolox (Fig. 5I). Importantly, FTE exhibited a significant upward shift in oxidative stress when cocultured with hrMSCs and not nMSCs, indicating that hrMSCs induce oxidative stress in adjacent FTE and are a potential source of hrMSC-mediated DNA damage (Fig. 5J).

Therefore, we next tested if neutralizing hrMSC oxidative stress would rescue DNA damage in FTE. We cocultured hrMSCs with FTE ±10 μmol/L Trolox and quantified 53BP1 foci in FTE. Trolox-treated cocultured FTE exhibited significantly less 53BP1 foci than DMSO control–treated cells (Fig. 5K), and thus, these data suggest that hrMSC oxidative stress contributes to FTE DNA damage, albeit by an unknown mechanism. We found that *WT1* overexpression also positively correlated with increased CellROX DR fluorescence in MSCs (Fig. 5L). Similarly, *WT1* overexpression in nMSCs resulted in a ~2.5-fold increase in CellROX DR fluorescence compared with empty vector controls (Fig. 5M), whereas *WT1* KD in hrMSCs slightly reduced oxidative stress compared with shRNA scramble control cells (Fig. 5N). Furthermore, nMSCs cocultured with tumor cells, as seen in Fig. 2K and L, exhibited not only increased WT1 expression but also a ~25% increase in CellROX DR fluorescence compared with nMSCs in monoculture (Fig. 5O and P). However, coculture with $P53^{null}$ FTE nonsignificantly increased nMSC ROS. These results were mirrored in hrMSC cocultures. Together, these data indicate that increased WT1 expression results in increased MSC oxidative stress. Moreover, neutralizing hrMSC oxidative stress blocks

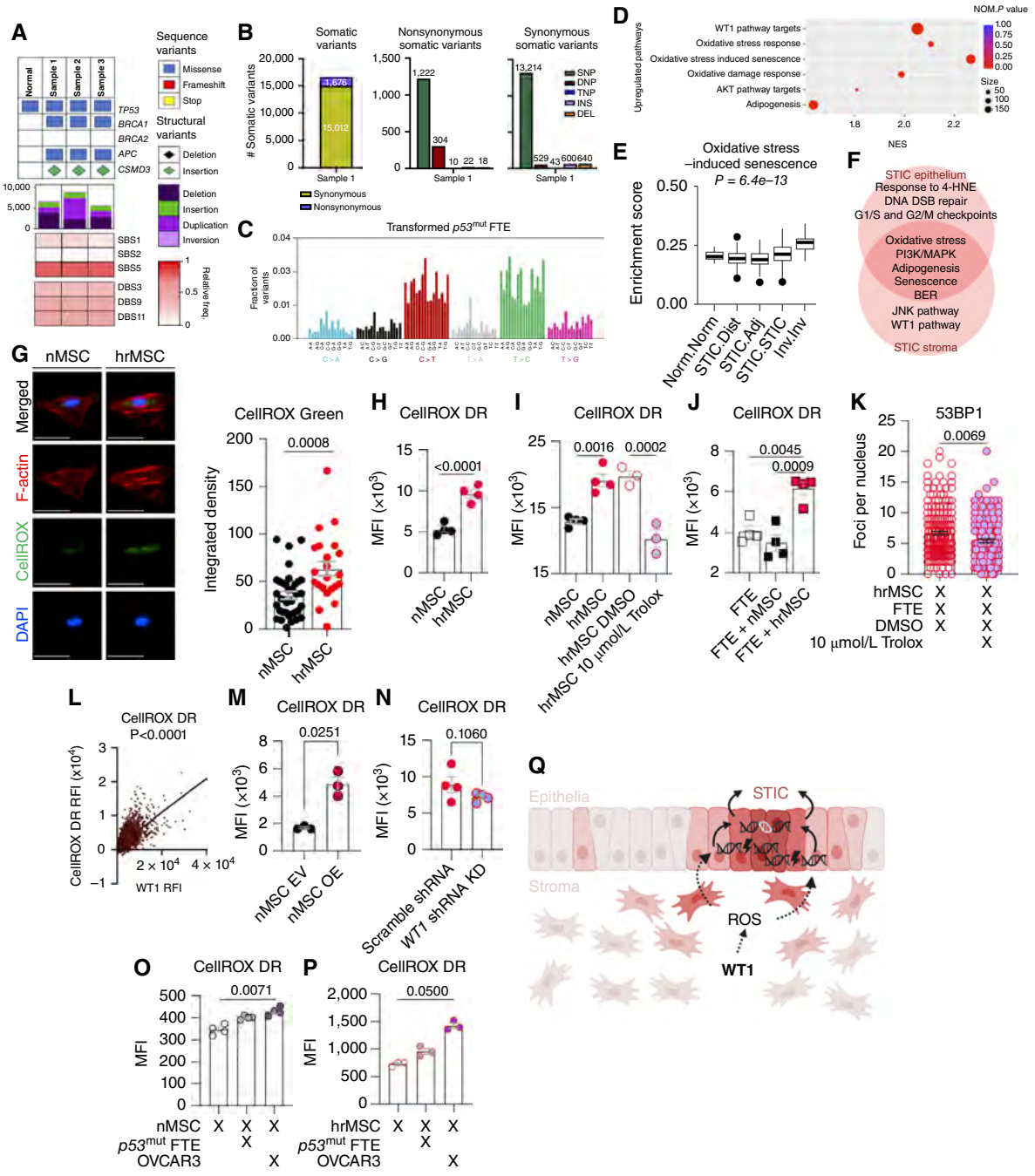

Figure 5. Transformed, metastasized *P53*^{null} FTE harbor mutational hallmarks of HGSOC. Whole-genome sequencing was used to characterize mutations present in transformed *P53*^{null} FTE originating from *P53*^{null} FTE/hrMSC organoids. **A,** Oncoprint including mutations in genes commonly mutated in HGSOC. This includes correlations to COSMIC single- and double-base signatures that are shown [single-base substitution (SBS) and double-base substitution (DBS), respectively]. **B,** Summary statistics of mutational analysis including somatic synonymous and nonsynonymous mutations. **C,** Representative graph of single-base mutations for one sample exhibiting the pan-cancer mutational signature (signature 5). **D,** Gene set enrichment analysis on STIC stroma relative to normal stroma from Fig. 1 DSP. **E,** Enrichment score of stromal genes associated with oxidative stress–induced senescence derived from our DSP dataset. **F,** Gene set enrichments shared between STIC stroma and STIC epithelium. **G,** IF and (**H**) flow cytometry of hrMSCs stained with the general oxidation probe CellROX Green and CellROX DR, respectively. Representative cells are shown at 20× magnification with a 100 μm scale bar. In **G** and **K**, individual data points correspond to individual nuclei. More than 3 fields per group were taken to analyze 150–200 individual cells. In **H**–**J**, individual data points correspond to separate wells. **I,** Flow cytometry analysis of MSC CellROX DR after treatment with the antioxidant Trolox. **J,** Flow cytometry analysis of carboxyfluorescein succinimidyl ester (CSFEL)-labeled FTE cells cocultured with MSCs ($n = 3$). MFI data were normalized for cell number. FTE CellROX values are displayed. **K,** 53BP1 foci per FTE nuclei after 24-hour coculture with hrMSCs ±10 μmol/L Trolox. **L,** Simple linear regression correlating WT1 relative fluorescence intensity (RFI) with CellROX DR determined by flow cytometry. Individual data points represent single cells. **M,** CellROX DR MFI following lentiviral overexpression of *WT1* in nMSCs. **N,** CellROX DR MFI following lentiviral shRNA KD of *WT1* in hrMSCs. **O,** FTE or ovarian cancer cells were cocultured with either CellTrace-labeled (**O**) nMSCs or (**P**) hrMSCs. MSCs were assessed for changes in CellROX DR fluorescence. For **G**–**P**, *P* values were determined by the Student's *t* test. **Q,** *WT1* overexpression induces MSC and FTE oxidative stress, resulting in increased FTE DNA DSBs.

hrMSC-induced DNA damage in cocultured FTE (Fig. 5Q). Further, the increased WT1 and ROS levels in hrMSCs can be driven by fully transformed HGSOC cells but not by premalignant FTE.

hrMSCs Produce Elevated Lipid Hydroperoxides Relative to Matched, Non–Tumor-supportive nMSCs

One consequence of increased oxidative stress is lipid peroxidation. Lipid peroxides can be trafficked between cells and break down into the mutagenic compounds malondialdehyde (MDA) and 4-hydroxy-2E-nonenal (4-HNE; refs. 21–23). We hypothesized that this may be a mechanism by which hrMSCs induce DNA damage in FTE. Indeed, both 4-HNE and MDA were increased in hrMSCs relative to nMSCs, which was abrogated following Trolox treatment (Fig. 6A–J). Like CellROX, both 4-HNE and MDA positively correlated with WT1 expression (Fig. 6E and J). To determine if lipid peroxides are trafficked from hrMSCs to FTE cells, we utilized both ELISA and IF assays to detect extracellular and intracellular MDA, respectively. Although MDA concentrations were near undetectable in the conditioned media of either nMSC or hrMSCs (Supplementary Fig. S6A), MDA puncta are visualized by IF both on and within the cell membrane of hrMSCs (Fig. 6K). Notably, these MDA puncta were present in/on the filopodia/nanotubes originating from CTV-labeled hrMSCs and connect to FTE, suggesting that the transfer of lipid peroxides occurred via direct interaction. To verify this, we labeled hrMSC lipids using BODIPY C12 and pretreated cells overnight with 5 μmol/L latrunculin B (Lat B). Lat B depolymerizes intracellular actin, thereby causing the loss of nanotubes (24, 25). CellTrace DR–labeled FTE were pulsed with BODIPY–labeled MSCs for 4 hours, after which FTE were collected and analyzed by flow cytometry. Lat B–treated hrMCSs trafficked significantly less lipids to cocultured FTE (Fig. 6L and M), thus implicating actin-based cellular bridges such as nanotubes as a source of lipid or lipid hydroperoxide transfer. Of note, treating hrMSCs with GW4869, an inhibitor of extracellular vesicle formation and release, did not alter the amount of transferred lipids (Supplementary Fig. S6B–S6D). These data suggest a direct transfer mechanism of lipids/lipid peroxides to the epithelium rather than an exosomal-mediated mechanism. FTE cells cocultured with hrMSCs exhibited significantly increased MDA and 4-HNE compared with FTEs cultured alone or with nMSCs (Fig. 6N and O). We next verified that exogenous lipid peroxide breakdown products could induce DNA DSBs in FTE. We treated FTE with 20 μmol/L 4-HNE for 8 hours and quantified 53BP1 foci. Indeed, 53BP1 foci were significantly increased in FTE treated with 4-HNE compared with DMSO vehicle–treated FTE cells (Fig. 6P). These data indicate that hrMSCs induce DNA DSBs in FTE, in part via the production and trafficking of lipid peroxide breakdown products (Fig. 6Q).

Loss of AMPK, an Important Redox Regulator, Mediates Development of the hrMSC Phenotype

We sought to clarify the mechanism by which hrMSCs upregulate WT1, leading to increased oxidative stress and the DNA damage–inducing phenotype. We investigated pathways with potential WT1 regulatory roles altered in both our DSP and DNA methylation array data. DSP data demonstrated multiple pathways associated with oxidative stress and AMP-associated protein kinase (AMPK) regulation. Further, methylation analysis demonstrated increased methylation in the promoter region of AMPK subunits (*PRKAG1* shown for reference; Fig. 7A; DEGs identified by DSP related to AMPK are included in Supplementary Table S2 and Supplementary Fig. S7A). Given this and a strong body of literature supporting oxidative stress in the setting of reduced AMPK alpha 1 (AMPKα1) activation, loss of feedback inhibition, as well as reduced AMPK being a well-characterized hallmark of aging (26, 27), we assessed alterations in AMPK at the mRNA level between nMSCs and hrMSCs. WT1 ddCq values were used to classify nMSCs or hrMSCs. We characterized the expression of AMPK subunits by qRT-PCR and found that hrMSCs, compared with nMSCs, exhibit a decrease in AMPK subunit and regulatory kinase (*CAMKK2* and *STK11*) expression, consistent with functional downregulation in the setting of promoter methylation (Fig. 7B). To date, a direct link between WT1 and AMPK expression has not been demonstrated. AMPK limits the phosphorylation of JNK at T182/183 (28). Also, JNK phosphorylation of c-JUN at S63/73 results in c-JUN binding at the *WT1* promoter and a subsequent increase in *WT1* transcription (29). Given that hrMSCs overexpress *WT1* and exhibit reduced AMPK subunit mRNA, we hypothesized that AMPK loss, likely through epigenetic silencing, facilitates WT1 upregulation by derepressing JNK/c-JUN signaling (Fig. 7C; the ratio of phospho:total protein as well as *WT1* ddCq values are shown in Supplementary Fig. S7B–S7F). When we compared AMPKα1 and phospho-AMPKα1 (T172; pAMPKα1; active form) protein expression between nMSC and hrMSC patient cell lines, we observed a significant reduction in the amount of both total and phosphorylated AMPKα1 in hrMSCs (Fig. 7D). There was no difference in the ratio of pAMPK to AMPK (Supplementary Fig. S7B and S7C), further suggesting that AMPK is downregulated at the transcriptional level in hrMSCs. Next, we characterized both total and phospho-JNK/c-JUN in nMSCs and hrMSCs. As expected, hrMSCs have increased phospho-JNK/c-JUN and total c-JUN (Fig. 7E and F; ratios are shown in Supplementary Fig. S7D and S7E). Importantly, both p-JNK ($r^2 = 0.3854$, $P = 0.1005$) and p-c-JUN ($r^2 = 0.5669$, $P = 0.0311$) expression positively correlate with WT1 expression by linear regression at an individual patient/sample level (Fig. 7G and H). As proof of concepts for age-related AMPK loss and JNK/c-JUN regulation of WT1 in hrMSCs, we assessed AMPK protein levels chronologically across MSC passages. We demonstrated AMPK loss with increased passage only in nMSCs (Fig. 7I). Additionally, hrMSC AMPKα1 levels started lower than nMSCs at the same passage and remained lower than levels in nMSCs at earlier passages. No clear differences were observed in phospho-AMPK (Supplementary Fig. S7G). Moreover, inhibiting JNK phosphorylation with the small molecular inhibitor SP600125 resulted in the loss of c-JUN phosphorylation at S63 with subsequent loss of WT1 expression (Fig. 7J). There was a dose-dependent effect of SP600125 on decreases in p-JNK at T182/183 and p-c-JUN and WT1, further validating the mechanistic link between JNK/c-JUN/WT1 in MSCs (Fig. 7J).

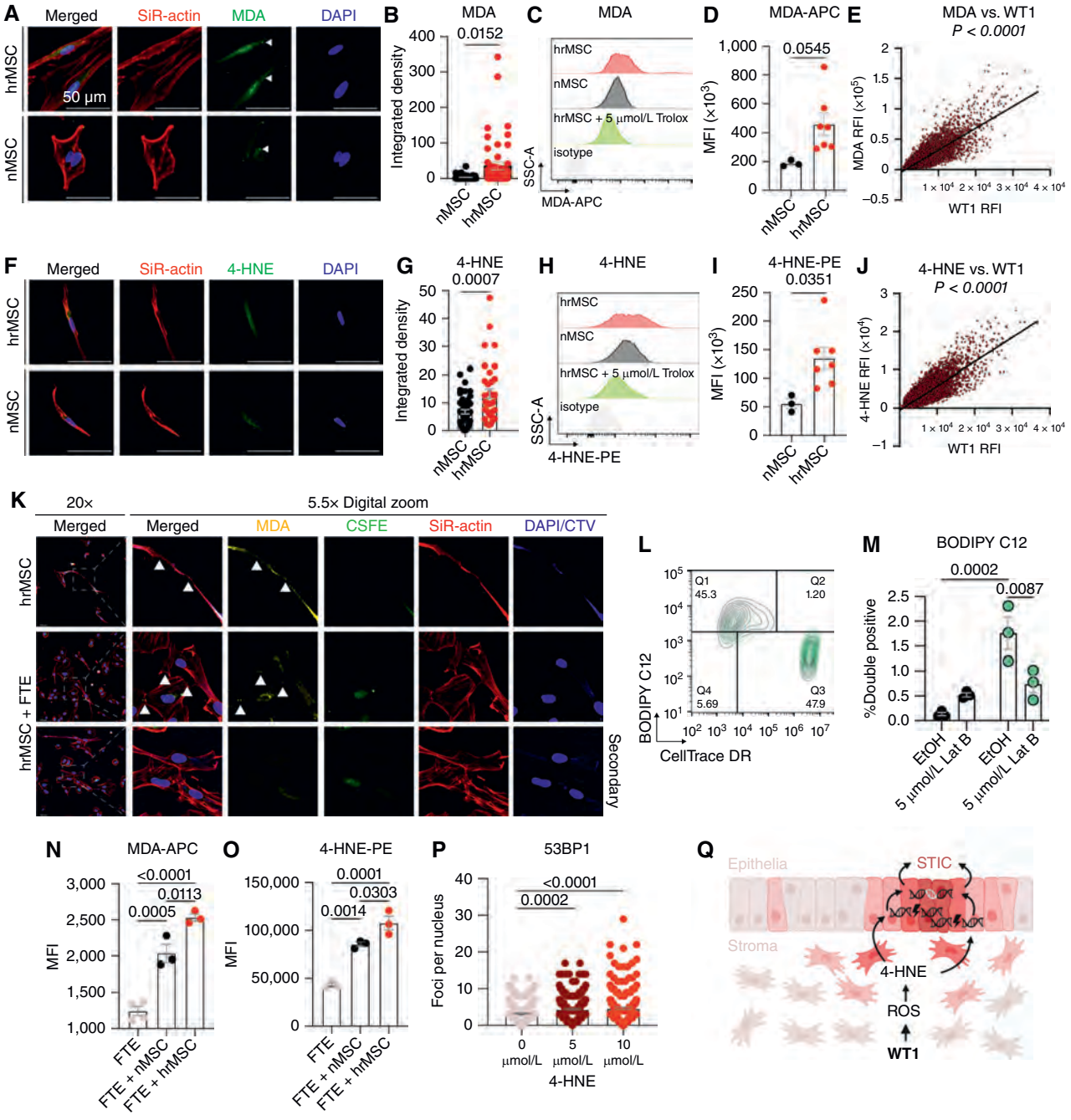

Figure 6. Increased oxidative stress in hrMSCs results in increased lipid peroxide breakdown products capable of inducing DNA DSBs in FTE. 4-HNE and MDA were compared between nMSCs and hrMSCs by fluorescence microscopy ($n = 3$) and flow cytometry ($n > 3$; **A–J**). Representative images at 20× magnification are shown. More than three fields were imaged and analyzed per condition. Silicon rhodamine (SiR) actin stain was used for cell masking. In **B** and **G**, each data point represents an individual cell, whereas in **D** and **I**, each data point represents the MFI of individual patient cell lines ($n = 3$ nMSC lines and $n = 7$ hrMSC lines). **C** and **H,** Stacked histograms of nMSCs, hrMSCs, and hrMSCs with 10 μmol/L Trolox treatment as a negative control. **E** and **J,** Flow cytometry was utilized to conduct a simple linear regression correlating WT1 expression with either MDA or 4-HNE. Individual points represent single cells. **K,** Representative images of MDA in hrMSCs (CTV⁺) that are cocultured with FTE (CT CSFE⁺). White arrowheads depict MDA puncta that are visible within nanotubule connections between cells ($n > 3$). **L** and **M,** Analysis of BODIPY C-12/CellTrace DR double-positive FTE after coculture with BODIPY C12-stained hrMSCs. hrMSCs were treated with 5 μmol/L Lat B or ethanol control overnight preceding coculture. Individual data points represent individual wells. Black circles represent FTE alone, and green circles are FTE with hrMSC coculture. %Double positive indicates FTE that received hrMSC-derived lipids. Quantification of (**N**) MDA-APC and (**O**) 4-HNE-PE MFIs in FTE cell monocultures or cocultured with nMSCs or hrMSCs. **P**, FTE were treated with 5–10 μmol/L 4-HNE and assayed for 53BP1 foci. Student *t* test was used to determine significance in all panels except **P**, where *P* values were determined by ordinary one-way ANOVA with Tukey's multiple comparison analysis. **Q,** Excessive stromal lipid peroxidation contributes to increased DNA damage in FTE.

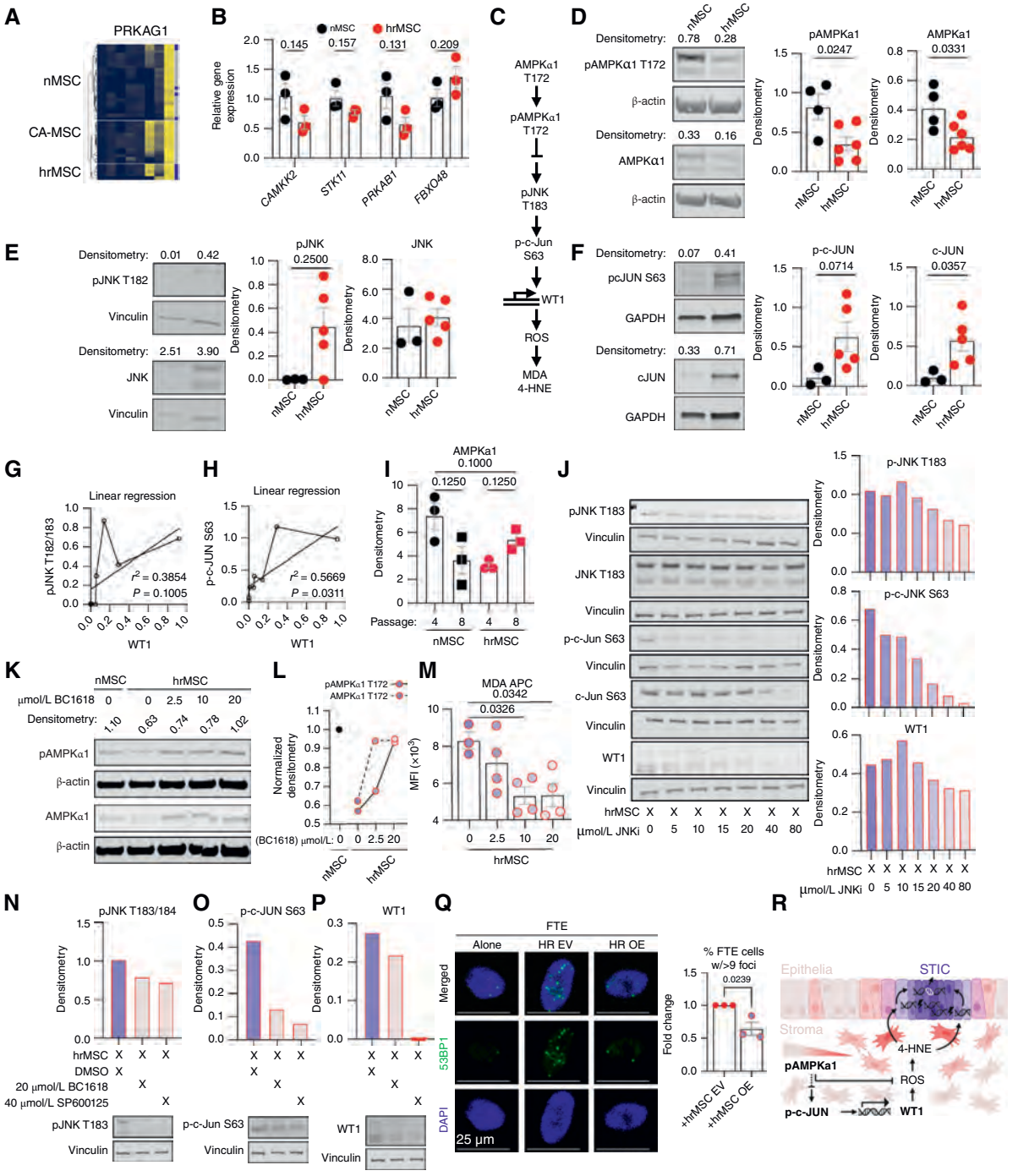

Figure 7. Aging-associated AMPK derepression of the JNK/c-JUN/WT1 axis results in the hrMSC protumorigenic phenotype. **A,** DNA methylation in nMSCs, hrMSCs, and CA-MSCs at the promoter region of the *PRKAG1* gene. **B,** qRT-PCR expression data of AMPK-related genes in nMSC vs. hrMSC. **C,** Hypothesized AMPK/JNK/c-JUN/WT1 axis. **D–F,** Characterization of phospho-AMPKα1 and total AMPKα1, JNK, and c-JUN in nMSCs and hrMSCs. Representative Western blots are shown with corresponding densitometries. Patient samples were grouped, and statistical significance was determined using the Student's *t* test. For both nMSCs and hrMSCs, $N > 3$ patients. **G** and **H,** Simple linear regressions correlating p-JNK and p-c-JUN with WT1 expression on a per-sample basis via densitometry. **I,** Quantification of AMPK Western blot levels in nMSC vs. hrMSC at passage 4 vs. passage 8. **J,** Western blot of hrMSCs treated with increasing doses of the JNK inhibitor SP600125. Quantified band intensities are shown. **K** and **L,** Western blot and quantification of AMPKα1 and pAMPKα1 following BC1618 treatment for 24 hours. **M,** BC1618-treated hrMSCs were analyzed by flow cytometry for MDA fluorescence. *P* values were determined by ordinary one-way ANOVA with Tukey's multiple comparison analysis. **M–P,** Quantification of p-JNK, p-c-JUN, and WT1 bands following treatment of hrMSCs with either BC1618 or SP600125. **Q,** Representative 20× images of FTE that were cocultured at a 1:1 ratio with hrMSC AMPKα1-m-GFP or empty vector (EV) transduced. The percentage of cells with >9 53BP1 foci was quantified by fluorescence microscopy. More than 3 fields per condition were taken to analyze 150–200 individual cells. The Student's *t* test was used to determine the significance of **Q**. **R,** Aging-associated loss of AMPK phosphorylation and expression results in the derepression of JNK phosphorylation, resulting in increased WT1 expression, oxidative stress, and FTE DNA DSBs.

Restoration of AMPK in hrMSCs Ameliorates hrMSC Oxidative Stress and Subsequent FTE DNA Damage Burden after Coculture

To test whether AMPK loss was responsible for the hrMSC phenotype, we both pharmacologically (Fig. 7K and L; Supplementary Fig. S7H–S7L) and genetically (Supplementary Fig. S7M–S7U) restored AMPK expression. When we restored AMPKα1 and pAMPKα1 expression pharmacologically using BC1618 (Fig. 7K and L), a small molecule inhibitor of pAMPKα1 ubiquitination and subsequent degradation, we observed dose-dependent decreases in total hrMSC MDA (Fig. 7M) and 4-HNE (Supplementary Fig. S7H) via flow cytometry. These trends held true for AMPKα1 OE hrMSCs (created via lentiviral transduction; Supplementary Fig. S7Q–S7S). Importantly, treating hrMSCs with either a single dose of 20 μmol/L BC1618 or 40 μmol/L SP600125 resulted in an equivalent reduction of p-JNK and p-c-JUN (Fig. 7N and O, respectively). BC1618 treatment resulted in a partial reduction of WT1, whereas treatment with SP600125 resulted in a complete loss of WT1 (Fig. 7P). Again, these results were mimicked in AMPK OE hrMSCs (Supplementary Fig. S7P) with the greatest reduction seen in *WT1* isoform A. Together, these data suggest that AMPKα1 restoration limits WT1 expression and subsequent hrMSC lipid peroxidation production. Thus, we hypothesized that AMPKα1 restoration and subsequent loss of WT1 expression ameliorate DNA damage in FTE. Indeed, after coculturing FTE cells with AMPKα1 OE hrMSCs, we observed a significant reduction in γH2AX (Supplementary Fig. S7T) and a 2-fold reduction in the population of FTE cells with abundant 53BP1 foci (>9 foci per nucleus; Fig. 7Q). Collectively, these data demonstrate that AMPKα1 loss derepresses the JNK/c-JUN axis, resulting in increased WT1 in MSCs and increased oxidative stress, lipid peroxidation, and DNA damage in FTE (Fig. 7R).

DISCUSSION

It is now recognized that the majority of HGSOC is derived from the FTE; therefore, the majority of studies have focused exclusively on FTE-intrinsic selective pressures for oncogenesis (7, 8, 28–30). Further, pathologic mutations in either *BRCA1* or *BRCA2* convey a 30- to 40-fold increased risk of developing HGSOC; therefore, most studies focus on patients with germline mutations in these genes. However, most HGSOC occurs in women without germline *BRCA1*/2 mutations, highlighting a critical need to elucidate a mechanism of ovarian cancer initiation that considers other, more broadly applicable factors (31).

Our work indicates a critical role for the fallopian tube stroma in ovarian cancer initiation. Using a combination of multispectral IF, digital spatial transcriptomic profiling, DNA methylation analysis, and flow cytometry, we identified and isolated a subset of MSCs that exist within the fallopian tube stroma of women without cancer that phenocopy fully cancer-educated CA-MSCs. CA-MSCs are characterized by their tumor-supportive functions; however, given that these MSCs were identified in women without cancer, we termed these cells hrMSCs. We demonstrated that hrMSCs exist within the fallopian tube stroma of women without HGSOC. hrMSCs were most abundant surrounding STIC lesions, which are considered the precursor lesion to HGSOC. Additionally, the presence of hrMSCs extended well beyond the boundaries of the STIC lesion, creating a possible field effect surrounding and contributing to the development of STIC lesions and, ultimately, HGSOC. Spatial transcriptomic data further supported the concept of a stromal field effect with the STIC stromal signature, which is strongly enriched in the stroma of invasive HGSOC and is also enriched well beyond the borders of the STIC lesion, even extending into regions over 2 cm away from the STIC. WT1 signatures also demonstrated enrichment in a location-dependent manner, supporting the role of hrMSCs in the development of a stromal field effect during HGSOC initiation. hrMSCs were also found in women without any identifiable pathology in their fallopian tubes and were enriched in patients of greater age and patients with germline *BRCA1*/2^{mut}; however, they were not exclusive to those subgroups. We also demonstrated that hrMSCs functionally mirror CA-MSCs in their ability to support tumor cell growth. Moreover, hrMSCs directly influenced benign FTE cells. hrMSCs increased DNA damage and DSB burden in FTE cells. This association was validated *in vivo*, with colocalization of FTE with 53BP1 foci (a marker of DNA DSBs) and hrMSCs within the underlying stroma. DNA DSBs are considered hallmarks of HGSOC, often directly contributing to the allelic copy number variations typical of invasive disease. Given the toxicity of DNA DSBs in human cells, we expected a total loss of epithelium after prolonged coculture or upon additional cell stress. Therefore, it was striking to discover that not only do FTE cells proliferate more when in coculture with hrMSCs, but FTE recover significantly better after additional oxidant stress when exposed to hrMSC conditioned media. These data indicate that hrMSCs provide two vital stimuli for ovarian cancer initiation: the induction of DNA damage and the promotion of epithelial survival. Additionally, hrMSCs may support the stem-like capacity of FTE by enriching cells with high ALDH expression and the capacity to grow in spheres. As many hypothesize that cancer initiation depends on the malignant transformation of the normal stem cell population, the impact of stromal-mediated DNA damage induction and survival may be even more potent when occurring in the FTE stem cell population (32).

Most importantly, hrMSCs triggered full malignant transformation of primary FTE cells *in vivo*. We validated malignant transformation by WGS, which demonstrated classic hallmarks of HGSOC. To date, the transformed epithelium has been passaged >80 times in comparison with primary epithelial lines that senesce within days or weeks of *ex vivo* culture, demonstrating permanent retention of malignant features resulting from hrMSC influence. Other sources of FTE DNA damage have been described; however, none have recapitulated *in vivo* transformation (33–35). These additional stressors may encourage the protumorigenic function of hrMSCs; therefore, future investigations into hrMSC metabolism, cell-to-cell interactions, and FTE DNA damage and cellular responses are vital in determining the precise mechanism of epithelial transformation. Also, it is important to note that these tumor initiation experiments were performed in a mammary fat pad model in an immune-compromised mouse. This model was chosen to allow easy palpation and avoid cell

manipulation (such as transduction with luciferase constructs) to avoid confounding results; however, there are important limitations, including a lack of an orthotopic microenvironment and immune response. Recapitulation of these results in a fully murine model is an important next step.

Our initial investigation into the mechanism of hrMSC-mediated malignant transformation was based on the genomic analysis of the transformed FTE, which demonstrated a mutational signature associated with chronic oxidative stress (COSMIC single-base signature 5). We then verified that hrMSCs have higher oxidative stress compared with nMSCs. This high oxidative stress leads to an increased burden of 4-HNE and MDA in hrMSCs. 4-HNE and MDA belong to two separate lipid peroxide breakdown product families, each capable of inducing genotoxic stress, either in the form of replication fork stalling or DNA DSBs. Lipid peroxides have been implicated in disease progression; however, their involvement in HGSOC initiation has been neglected. We also demonstrate that hrMSCs lose expression of AMPKα1, likely through epigenetic silencing. AMPK loss results in increased JNK/c-JUN signaling that transcriptionally upregulates WT1, thus driving the hrMSC phenotype. Further, AMPK loss results in reduced responsivity to fluctuations in cellular oxidative stress. This suggests that hrMSCs lack robust oxidant stress feedback inhibition, which would permit hrMSCs to accumulate 4-HNE/MDA and induce DNA damage in FTE. Intriguingly, pharmacologic and genetic restoration of AMPKα1 in hrMSCs or hrMSC treatment with Trolox, a lipid peroxide-specific antioxidant, resulted in significantly lower oxidative stress, 4-HNE/MDA burden, and FTE DNA DSBs. Further work is needed to understand the mechanism driving epigenetic silencing of AMPKα1 in hrMSCs, how hrMSCs both induce DNA damage yet increase FTE survival, and other related or orthogonal mechanisms underlying hrMSC-mediated FTE transformation.

Collectively, this work identifies the stromal microenvironment as a crucial factor in HGSOC initiation. We demonstrate that benign resident MSCs take on a protumorigenic phenotype prior to the initiation of cancer and that these cells actively participate in the malignant transformation of associated epithelial cells. This information is vitally important to our understanding of how HGSOC forms and in the effort to create early detection or prevention strategies for this deadly disease. To date, biomarkers associated with HGSOC have not reached the necessary sensitivity and specificity to be useful for the early detection of ovarian cancer. Understanding the role of the fallopian tube stroma in HGSOC initiation may enable the discovery of stroma-based biomarkers to improve the development of methods for early detection. Similarly, stroma-based prevention strategies may also be possible to block the tumor-promoting impact of hrMSCs. This work highlights the importance of the stromal microenvironment in HGSOC initiation and provides support for investigating similar stroma-mediated functions at other sites of oncogenesis.

METHODS

nMSCs/hrMSCs

MSCs were isolated from the fallopian tubes of women with or without *BRCA* mutations undergoing gynecologic surgery for benign indications or risk-reducing salpingo-oophorectomies, without findings of cancer or precancerous lesions upon standard pathologic examination. Using previously described protocols, fresh fallopian tubes were cut into <1 mm^3 pieces and plated in six-well plates (13). Following the International Society for Cell and Gene Therapy (ISCT) guidelines on the minimal criteria for defining multipotent MSCs, MSCs were selected for plastic adherence and cell surface marker expression ($CD105^+$, $CD90^+$, $CD73^+$, $CD45^-$, $CD34^-$, $CD14^-$, $CD19^-$; ref. 36). Adipocyte, osteocyte, and chondrocyte differentiation capacity was also verified. MSCs were propagated using Mammary Epithelial Cell Basal Medium supplemented with 10% heat-inactivated FBS, 1× B27, 20 ng/mL EGF, 1 ng/mL hydrocortisone, 5 μg/mL insulin, 100 μmol/L β-mercaptoethanol, 10 ng/mL β-FGF, 1% penicillin–streptomycin, and 20 μg/mL gentamicin. MSCs were used for functional experiments for at most, 8 to 10 passages. For pharmacologic experiments, BC1618 (provided by the Finkel Lab; treated at a range of 0–20 μmol/L), SP600125 (Sigma Aldrich; 25567; treated at a range of 0–80 μmol/L), and GW4869 (MedChemExpress; HY-19363; treated at a range of 0–40 μmol/L) were diluted in DMSO. Lat B (Millipore Sigma; L5288; treated at a range of 0–5 μmol/L) was diluted in 100% ethanol.

FTE

Using fresh normal human fallopian tube tissue, FTE were isolated following a modified version of a previously described protocol (37). Briefly, fresh tissue was mechanically and enzymatically dissociated into a single-cell suspension, plated, and passaged on plates coated with tissue culture–treated placental collagen IV (Sigma Aldrich; C7521). The single-cell suspension was then cultured in a DMEM/Ham's F-12 50:50 mix supplemented with 2% Ultroser G serum substitute and 1% penicillin–streptomycin. FTE cells were validated for expression of panCK and were negative for MSC markers CD105, CD90, and CD73. Immortalized FT190 control cells were donated by Ronny Drapkin (RRID:CVCL_UH57) and were utilized in parallel where possible. For all adherent and nonadherent coculture experiments, FTE cells were plated at a 1:1 ratio with MSCs. This ratio was chosen because FTE rapidly undergo replicative senescence in *ex vivo* culture. Higher ratios of FTE to MSCs resulted in poor FTE growth kinetics.

DSP

NanoString's DSP GeoMx platform (RRID:SCR_021660) was used for spatial transcriptomics and conducted in the UPMC Hillman Cancer Center Cytometry Facility. Samples include $N = 22$ fallopian tubes with STIC, $N = 6$ fallopian tubes with invasive HGSOC, and $N = 4$ fallopian tubes without pathology. Slides were incubated with the Whole Transcriptome Atlas library prior to collection. For collection, the GeoMx platform was utilized to select regions of interest (ROI) on the slides. The strategy for segmenting discrete regions by morphology marker within ROIs is as follows: epithelium: $CD45^-$ and $panCK^+$ and stroma: $CD45^-$, $CD20^-$, and $panCK^-$. STIC regions were confirmed with p53 staining and verified by a gynecologic pathologist (T.R. Soong). Antibodies used for localization are as follows: anti-human CD45 BUV395 (BD Biosciences, Cat# 563792, RRID:AB_2869519), anti-human panCK (Santa Cruz Biotechnology, Cat# sc-81714, RRID:AB_2191222), and anti-human CD20 Spark NIR 685 (BioLegend, Cat# 302366, RRID:AB_2860775).

Ninety-six-well plates were collected and sent for sequencing at the UPMC Genomics Core Facility (RRID:SCR_025357) using standard protocols. Data normalization, quality control, and analysis were conducted by the UPMC Hillman Cancer Bioinformatics Services (RRID:SCR_025356). Sequencing files were converted from FastQ to digital count conversion format using the GeoMx NGS Pipeline. The sequencing saturation was 87% ± 2% (mean ± SEM). Reads were processed to clip adaptors, merge overlapping mates, align to the Readout Tag Sequence-ID barcodes, and remove PCR duplicates using unique molecular identifiers. The result-

ing read count matrix was passed through a robust quality control procedure to remove ROIs of low surface area (<3,000 μm²) or low perfectly aligned reads (<80%) and probes of low quality or identified as global or local outliers (failing the Grubbs outlier test in ≥20% of segments). The remaining data were upper quartile normalized and $\log_2$-transformed. Genes of low expression (<5.2, based on the distribution of negative probe expression) were removed prior to statistical comparisons. Gene set enrichment analysis was conducted on DEGs extracted from DSP data between STIC and normal stroma and epithelium using the Broad Institute's GSEA 4.3.3 software (RRID:SCR_016863; refs. 38, 39).

Methylation Data Processing

EPIC array intensity data (IDAT) files from GSE138072 were combined with an additional 12 EPIC array samples for a dataset of 14 FT, 23 omental, and 7 ovarian samples ($N = 44$ total samples). These samples were further differentiated as nMSCs ($N = 20$), CA-MSCs ($N = 14$), and hrMSCs with heterozygous *BRCA* mutations ($N = 10$). IDATs were processed using sesame version 1.8.2 with the openSesame function (RRID:SCR_002849) and default parameters (40). Array probes were excluded if they had more than 10% missing data across all samples; this resulted in the exclusion of 474,808 probes.

Probe Selection

The top 1,000 probes with the largest average increase in methylation in CA-MSCs relative to nMSCs, as well as the 1,000 with the largest average decrease in methylation in CA-MSCs, were selected as these probes best discriminate between nMSCs and CA-MSCs. hrMSCs were not included in this probe selection. All samples were included in the selection of the top variable probes, which were selected by ranking the standard deviation across all samples.

UMAP analysis was done using the uwot package version 0.1.14 (41). The UMAP was done using the top discriminating probes for CA-MSC–MSC, scaled with a column mean of 0 and a variance of 1. The umap function was run with default parameters, except that the spread option was set to 2, and the effective minimum distance between embedded points was set to 0.001. Heatmaps were generated using ComplexHeatmap version 2.14.0 (RRID:SCR_017270; refs. 40, 41).

FTE Proliferation Assay

FTE cells were stained with CTV (Invitrogen C34571) following the manufacturer's protocol. CTV-labeled FTE cells were cultured alone or cocultured with nMSCs or hrMSCs in a 12-well plate at a 1:1 ratio. Cells were counted daily for 4 days using a hemocytometer. The percentage of CTV-labeled FTE cells in coculture was determined by flow cytometry. Total FTE cells (CTV-labeled) = total cell number × CTV positive cell %.

Sphere Formation Assay

Primary FTE cells were stained with CTV, following the manufacturer's protocol. Using ultralow-adherence 96-well plates, labeled FTE were cultured alone (1×10^3 cells/well), with hrMSCs (1×10^3 total cells/well), or with nMSCs (1×10^3 total cells/well) in 300 μL Mammary Epithelial Cell Basal Medium supplemented with 1× B27, 20 ng/mL EGF, 1 ng/mL hydrocortisone, 5 μg/mL insulin, 100 μmol/L β-mercaptoethanol, 10 ng/mL β-FGF, 1% penicillin–streptomycin, and 20 μg/mL gentamicin. Spheres were counted in the entire well at 7 days after plating (>4 cells per spheroid, at least 1 FTE per sphere).

ALDH Assay

Primary FTE or FT190 FTE ALDH activity was determined with the ALDH-based cell detection kit (STEMCELL Technologies). FACS gating was based on live cells (via propidium iodide) with a diethylaminobenzaldehyde (DEAB) control for each sample. The percentage of ALDH⁺ primary FTE cells or FT190 control cells was determined by flow cytometry after 5 days of adherent coculture with or without nMSCs or hrMSCs. FTE was labeled with CTV to distinguish it from MSCs. Primary FTE and immortalized FT190 control cells were cocultured for 24 hours, either alone or with nMSCs or hrMSCs.

Cell Adhesion Assay

nMSCs, hrMSCs, or CA-MSCs were cultured overnight in a 12-well plate to form a monolayer. 3×10^4 HGSOC tumor cells including OVSAHO cells (RRID:CVCL_3114), OVCAR3 (RRID:CVCL_0465) cells, or pt412 cells (provided by Ronald Buckanovich), were stained with CTV and then added to the cultured nMSCs, hrMScs, or CA-MSCs. After 30 minutes, the cells were washed twice with PBS, and the attached CTV-labeled HGSOC cells were counted using a fluorescence microscope. Experiments were repeated independently three times per tumor cell type. For our positive control, wells were coated with PDL (Gibco, Cat# A3890401) at a concentration of 50 μg/mL in sterile Dulbecco's PBS. After a 1-hour incubation with PDL, the wells were washed thrice with distilled water and allowed to air dry in a laminar flow hood. Both epithelial and tumor cells were seeded onto both untreated and PDL-coated wells. Following a 30-minute incubation at 37°C, the wells were washed twice with Dulbecco's PBS. Cell adhesion was visualized using a Leica LAS-X Thunder microscope and quantified by cell counting with ImageJ (RRID:SCR_003070) software.

qRT-PCR

Using the RNeasy Mini Kit and on-column DNase treatment (Qiagen, Cat# 28106), RNA was isolated from MSCs. Samples were then processed for cDNA synthesis using the SuperScript III First-Strand Synthesis System (random hexamer; Invitrogen, Cat# 18080–051). SYBR Green–based RT-qPCR (Applied Biosystems, Cat# 4472908) was performed using the CFX96 Real-Time System, with GAPDH as the reference gene. Samples were run for 40 cycles.

Flow Cytometric Analysis

For quantification of WT1 expression, MSCs were washed with PBS, trypsinized into a single-cell suspension, and counted. MSCs were processed using the intracellular fixation and permeabilization buffer set (eBioscience; 88-8824-00). Briefly, 1×10^6 cells were resuspended in intracellular fixation buffer and fixed at room temperature (RT) for 20 minutes. Cells were washed twice with IC permeabilization buffer and subsequently stained with mouse anti-human WT1 405 (R&D Systems, Cat# IC57291V, RRID:AB_3656166; 1:100) for 20 minutes at RT, protected from light. MSCs were washed twice with IC permeabilization buffer, resuspended in FACS buffer, and analyzed using the CytoFLEX 4L cytometer. Ovarian cancer cell lines (e.g., OVCAR3) and primary CA-MSC cell lines were used as positive controls (13, 42–46). Where possible, data were gated using a similar baseline strategy of SSC-A/FSC-A>FSC-H/FSC-A>DAPI negative to accurately analyze live cell singlets. A minimum of 5,000 events were recorded for each sample. All MSC cell lines were validated using mouse anti-human CD105 FITC (BD Biosciences, Cat# 561443, RRID:AB_10714629), mouse anti-human CD90 PE (BD Biosciences, Cat# 555596, RRID:AB_395970), and mouse anti-human CD73 APC (BD Biosciences, Cat# 560847, RRID:AB_10612019).

For quantification of the CellROX (Life Technologies; C10448) oxidation probe, minor adjustments were made to the manufacturer's protocol. Briefly, MSCs were treated with complete media ±50 to 100 μmol/L hydrogen peroxide and 1 to 10 μmol/L Trolox for 30 minutes. Afterward, MSCs were rinsed with complete media and stained with 5 μmol/L of the CellROX DR probe for 30 minutes at 37°C. MSCs were rinsed 3 times with PBS and processed using the IC-Flow kit as described above. MSCs were run on the cytometer within the

suggested 2-hour interval. To correlate WT1 expression with CellROX DR, MSCs were stained with WT1 conjugates for 20 minutes after permeabilization.

For quantification of 4-HNE, we relied on commercially available 4-HNE antibody conjugates. Briefly, MSC controls were pretreated with either 50 to 100 μmol/L hydrogen peroxide or 5 to 10 μmol/L Trolox for 30 minutes. Afterward, MSCs and their controls were rinsed with complete media and processed using the IC-Flow kit. After permeabilization, MSCs were stained with mouse anti–4-HNE (Thermo Fisher Scientific, Cat# MA5-45792, RRID:AB_2932246; 1:100) or with mouse anti-MDA (Thermo Fisher Scientific, Cat# MA5-45801, RRID:AB_2932255; 1:100)–conjugated antibodies for 20 minutes at RT. Cells were rinsed with 1× PBS 3 times and analyzed using the CytoFLEX 4L cytometer.

Vectra Multispectral Imaging and Analysis

For the multispectral IF experiments, Akoya Biosciences' Vectra MOTiF imaging pipeline and reagents were used (RRID:SCR_025828). Auto-staining of the panels was carried out on a Leica BOND RX stainer, and the resulting stained slides were scanned using a Vectra Polaris imager. Subsequently, digital image files in QPTIFF format were downloaded and unmixed using Akoya Biosciences' inForm software. QuPath software was utilized to identify ROIs for phenotype analysis.

To quantify nMSC and hrMSC populations from our samples, we used QuPath version 0.3.2 image analysis software (RRID:SCR_018257). MOTiF qptiffs were loaded into QuPath. Cell segmentation was performed based on nuclei (DAPI). We created a cell classifier, detecting cells that were positive or negative for the antibodies of interest (CD90, CD45, CD73, CD105, WT1, and panCK). Anti-human antibodies used included: WT1 (Santa Cruz Biotechnology, Cat# sc-393498, RRID:AB_2905496), CD73 (Abcam, Cat# ab133582, RRID:AB_3674653), CD105 (Abcam, Cat# ab114052, RRID:AB_10900113), CD45 (Atlas Antibodies, Cat# AMAb90519, RRID:AB_2665572), CD90 (Novus, Cat# NBP1-43379G, RRID:AB_3209185), and panCK (Santa Cruz Biotechnology, Cat# sc-81714, RRID:AB_2191222).

The classifier was used to generate a phenotype algorithm applied to our cohort. We established that nMSCs had to be negative for CD45 and panCK and positive for three MSC markers (CD90, CD73, and CD105) and negative for WT1, whereas CA-MSCs were negative for CD45 and panCK, positive for the same three MSC markers (CD90, CD73, and CD105), and positive for WT1. We quantified the nMSCs and hrMSCs, normalized to the area of the analyzed ROI.

DNA Damage Assay

NMSCs and hrMSCs were passaged until they were 40% to 60% confluent. For conditioned media experiments, MSC medium was replaced with complete MSC medium 24 hours prior to FTE treatment. At this time, primary FTE or FT190 control cells were seeded in chamber slides. FTE cells were allowed to adhere overnight. After 24 hours, MSC conditioned medium was spun down at 4°C, 1,500 rpm for 5 minutes to remove cells and cellular debris. FTE media was then replaced with the processed conditioned media. FTE cells were incubated in conditioned medium for up to 4 hours and then assayed for γH2AX (Millipore, Cat# 05-636, RRID:AB_309864; 1:200) fluorescence intensity and 53BP1 (Abcam, Cat# ab175933, RRID:AB_2890610; 1:200) foci by IF. For coculture experiments, 40% to 60% confluent MSC cultures were dissociated and seeded with FTE or FT190 control cells at a 1:1 ratio and allowed to adhere overnight. Twenty-four hours after coculture, cells were assayed for γH2AX intensity and 53BP1 foci by IF.

FTE Recovery Assays

Patient-derived primary FTE cells or FT190 control cells were plated in 96-well plates. Twenty-four hours later, cells were treated with 50 mmol/L H_2O_2 for 10 minutes at RT. Cells were rinsed with PBS and supplemented with processed conditioned medium. Where possible, nMSCs and hrMSCs from the same patient were matched to limit confounding. Every 2 days, FTE medium was replaced with fresh, processed conditioned medium. RT MTS reagent (CellTiter 96 AQ_{ueous} One Solution; Promega; G3582) was added to each well, using a multichannel pipette per the manufacturer's recommendations. Cells were incubated with the MTS reagent at 37°C for 4 hours. Absorbance was read on a plate reader at 490 nm.

Immunofluorescence/IHC Staining

Cells were seeded in chamber slides and harvested at 24 hours. For γH2AX staining, cells were preextracted for 1 minute with preextraction buffer (0.6 mol/L EGTA, 0.5 mol/L PIPES, 0.5 mol/L $MgSO_4$, 3.0 mol/L KCl, 1% Triton X) and then fixed for 20 minutes with ice-cold 4% paraformaldehyde in PBS. Preextraction was omitted for 53BP1 foci and MDA/4-HNE experiments. Cells were washed twice with PBS and permeabilized with 0.5% Triton X in PBS for 10 minutes at RT. MDA/4-HNE experiments were permeabilized with 0.1% Triton X in PBS. Cells were washed twice with PBS and then blocked for 1 hour at RT with 100% SuperBlock (Thermo Fisher Scientific; 37535). Primary antibodies for DNA damage assays were diluted in PBS with 10% SuperBlock at the following dilutions: anti-human γH2AX Ser139 (Millipore, Cat# 05-636, RRID:AB_309864; 1:200), goat anti-mouse IgG AF546 (Thermo Fisher Scientific, Cat# A-11030, RRID:AB_2737024; 1:2,000), anti-human 53BP1 (Abcam, Cat# ab175933, RRID:AB_2890610; 1:200), goat anti-rabbit IgG AF488 (Abcam, Cat# ab150077, RRID:AB_2630356; 1:4,000), and donkey anti-rabbit AF647 (Abcam, Cat# ab150063, RRID:AB_2687541; 1:4,000). Cells were stained for 1 hour at RT and then washed six times with PBS. Secondary antibodies were diluted as above and incubated on cells for 1 hour at RT. Cells were washed six times with PBS, mounted with ProLong Diamond Antifade Mountant with DAPI (Invitrogen; P36962), and allowed to dry overnight, protected from light.

For experiments utilizing the CellROX Green stain, cells were initially stained with live cell F-actin (Spirochrome; SC001) for 1 hour at 37°C. Cells were washed 3 times with PBS and stained with 5 μmol/L CellROX Green in PBS for 30 minutes. Cells were processed per the manufacturer's recommendations. Briefly, cells were fixed in IC fixation buffer and mounted using ProLong Diamond Antifade Mountant with DAPI. MSC controls were pretreated with either 50 to 100 μmol/L hydrogen peroxide or 5 to 10 μmol/L Trolox for 1 hour. Cells were rinsed 3 times with PBS and subsequently fixed with 4% paraformaldehyde for 20 minutes at RT. Afterward, MSCs and their controls were stained with F-actin, rinsed 3 times with PBS, and mounted with ProLong Diamond Antifade Mountant with DAPI. Slides were imaged on a Leica Thunder DMi8 fluorescent microscope within 24 hours of staining.

Image Quantification. All slides were imaged on a Leica Thunder DMi8 fluorescent microscope. All images were deconvolved prior to quantification in ImageJ (RRID:SCR_003070). For image quantification, three or four random fields containing 150 to 200 individual cells were taken, using the 20× objective for each condition. Fluorescence intensity (integrated density) for nuclear γH2AX foci, cytoplasmic 4-HNE, and cytoplasmic MDA was quantified using ImageJ. 53BP1 foci per nucleus were also quantified using ImageJ.

Lentiviral Transduction

Lentiviral particles encoding *PRKAA1*-m-GFP (RC218572L2V), empty vector m-GFP control constructs (PS100071V/PS100093V), WT1-A-m-GFP (RC220079L4V), WT1 shRNA m-GFP (TL300442V), and scramble shRNA (TR30021V) were purchased from OriGene. Briefly, 2.5–3 × 10^4 hrMSCs were transduced with a multiplicity of infection of 10 to 50 viral particles per cell. Empty vector or scramble shRNA viral particles at a multiplicity of infection of 10 to 50 were

used as negative controls. Virus medium was removed 24 hours after transduction, and cells were allowed to recover until they were 70% confluent (1–2 days). Cells were passaged and sorted when applicable on m-GFP using a Sony MA900 multiapplication cell sorter. GFP$^+$ cells were validated for AMPKα1 overexpression by Western blot and allowed to rest for at least 24 hours prior to experimental setup. Validation of WT1 overexpression or KD was completed using intracellular flow cytometry.

Western Blotting

Western blot was used to quantify the amount of total and phosphorylated (T172) AMPKα1. MSCs were rinsed with 1× PBS and centrifuged at 1,500 rpm for 5 minutes at 4°C. Pellets were lysed with RIPA (Thermo Fisher Scientific; 89900) containing 1× phosphatase inhibitor (Roche; 04906837001) and 1× protease inhibitor (Roche; 11697498001) for 30 minutes on ice. Lysates were centrifuged at 13,000 × *g* for 5 minutes at 4°C. Supernatants were collected, and protein content was determined by BCA (Thermo Fisher Scientific; 23227). Thirty micromoles per liter of protein per sample was linearized with 1× lithium dodecyl sulfate (LDS) sample buffer (Invitrogen; NP0007) and loaded into 4% to 12% Bis-Tris precast gels (Invitrogen; NW04125). Samples were electrophoresed for 1.5 hours at 115 V and transferred onto nitrocellulose membranes (Cytiva; 10600001) using the Thermo Fisher Scientific semi-wet transfer apparatus. Membranes were blocked for 1 hour at RT using TBS Licor Buffer (927-60001) with 0.01% Tween 20 and then stained using rabbit anti-human pAMPKα1 (Cell Signaling Technology, Cat# 2535, RRID:AB_331250; 1:500), rabbit anti-human AMPKα1 (Cell Signaling Technology, Cat# 2532, RRID:AB_330331; 1:500), rabbit anti-human WT1 (Abcam, Cat# ab89901, RRID:AB_2043201; 1:1,000), rabbit anti-human p-JNK T182/183 (Cell Signaling Technology, Cat# 9251, RRID:AB_331659; 1:1,000), rabbit anti-human JNK (Cell Signaling Technology, Cat# 9252, RRID:AB_2250373; 1:1,000), rabbit anti-human p-c-JUN S63 (Cell Signaling Technology, Cat# 2361, RRID:AB_490908; 1:1,000), rabbit anti-human c-JUN (Cell Signaling Technology, Cat# 9165, RRID:AB_2130165; 1:1,000), rabbit anti-human vinculin (Cell Signaling Technology, Cat# 4650, RRID:AB_10559207; 1:1,000), rabbit anti-human GAPDH (Cell Signaling Technology, Cat# 2118, RRID:AB_561053; 1:5,000), and rabbit anti-human β-actin (Abcam, Cat# ab8227, RRID:AB_2305186; 1:2,000) overnight, rocking, at 4°C. Membranes were washed 3 times with 0.01% TBS-T and stained with goat anti-rabbit IR Dye 800CW (LI-COR Biosciences, Cat# 926-32211, RRID:AB_621843; 1:10,000) or donkey anti-mouse IR Dye 680RD (LI-COR Biosciences, Cat# 926-68072, RRID:AB_10953628; 1:10,000) for 1 hour at RT. Membranes were washed 3 times with 0.01% TBS-T and imaged using an Odyssey CLx fluorescence imaging system. Band densitometry was determined in ImageJ.

Mouse Model Tumor Initiation

Experimental procedures were performed in accordance with the protocol approved by the Institutional Animal Care and Use Committee at the University of Pittsburgh. Six- to eight-week-old female NSG (RRID:IMSR_JAX:005557) mice were used to assess tumor initiation capacity. Long-term organoids were grown using FTE containing *P53*^{null} mutation FTE, pathologic *BRCA1* mutation FTE, or FTE from patients who were not genotyped. The latter group of patients failed to meet mutation screening criteria (e.g., family history of *BRCA1/2* mutation or associated cancers) and are thus considered to be clinically WT. Organoids were originally generated with FTE cells alone or in coculture with hrMSCs or nMSCs and were allowed to grow for 4 to 10 weeks prior to injection. Organoids were dissociated and counted using a hemocytometer and trypan blue to get an estimate of cells per organoid. Each mouse was injected with organoids containing approximately 600 to 3,000 cells, depending on the number of cells obtained at the time of injection. Cells were injected into the inguinal mammary fat pad of NSG mice to allow us to palpate tumors. Mice were monitored by palpating the injection site for tumor initiation on a weekly basis and validated by tumor resection, H&E, and panCK IHC. For secondary initiation studies, the primary *P53*^{null} tumors and two metastases were grown *ex vivo*. Mouse cells were depleted (see "Mouse Cell Depletion"), and 0.5×10^6 transformed FTE cells were injected into the ovarian bursa of 6- to 8-week-old female NSG mice (47). IVIS imaging was conducted per our previously published protocol (47). Tumor growth was monitored for 7 weeks at which time tumors were dissected out and sent for histology.

Mouse Cell Depletion

Mouse cells were depleted from the xenograft tumor to enrich for human cells using the Mouse Cell Depletion Kit (Miltenyi Biotec, 130-104-694) as previously described (48). Briefly, tumor tissues were mechanically and enzymatically dissociated into a single-cell suspension. After determining the number of isolated cells, the cells were resuspended in 80 μL of buffer (1× PBS with 0.5% BSA) per 2×10^6 tumor cells and 20 μL of the magnetic labeling reagent for mouse cells. The cells were then incubated at 4°C for 15 minutes. After incubation, the sample volume was adjusted to 500 μL using buffer and run through large separation (LS) columns for magnetic separation. The flow-through containing purified human cells was collected, and the cells were then cultured and propagated using DMEM supplemented with 10% FBS and penicillin–streptomycin (penicillin: 100 U/mL and streptomycin: 0.1 mg/mL).

DNA Isolation

The isolated postinitiation and matched preinitiation FTE were processed for DNA isolation using the Qiagen DNeasy Blood and Tissue Kit (Cat# 69504), following the manufacturer's protocol.

Whole-Genome Sequencing

Sequence libraries were generated from isolated postinitiation and matched preinitiation FTE using the Illumina WGS DNA Prep workflow (Illumina) and subsequently sequenced on the Illumina NovaSeq 6000 platform (RRID:SCR_016387) with a minimum coverage of 50× and 30×, respectively. FASTQ files were filtered for quality using FASTQC (version 0.11.8; RRID:SCR_014583) and contaminants using FastQ Screen (version 0.11.4) and trimmed of adapters, N content, and low-quality bases [ea-utils (version 1.04); RRID:SCR_005553]. Quality FASTQ files containing paired-end clean reads were then mapped to the hg38 human reference genome with Burrows-Wheeler Aligner (version 0.7.17; RRID:SCR_010910), and the resulting BAM files were sorted, merged by lane, and duplicate reads marked using Sambamba (version 0.6.7; RRID:SCR_024328) and Picard (version 2.18.9; RRID:SCR_006525; refs. 49, 50). GATK BaseRecalibrator (version 4.4.0.0; RRID:SCR_001876) was used to adjust bases (51).

SNP and Short INDEL Variant Calling

GATK HaplotypeCaller (version 4.4.0.0) was used on preinitiation FTE BAM files to call germline base substitutions and short INDEL variants, which were quality filtered and annotated according to the GATK Best Practices Pipeline (52). Filtered germline variant call format files were used as the "panel of normals" for GATK MuTect2 (version 4.4.0.0) somatic variant calling. Two variant callers were employed to call somatic base substitutions and short indels, using the preinitiation FTE samples as normal: GATK MuTect2 (RRID:SCR_000559) and Strelka2 (version 2.9.10; RRID:SCR_005109), both using default parameters in tumor-normal mode (53). Variant calls were normalized

and decomposed using vt (version 0.58), merged using GATK CombineVariants, and left trimmed using vt (54). Variants that passed both callers and had at least five supporting reads and bidirectional read support were deemed variants of high confidence; these variants were functionally annotated using GATK Funcotator (version 4.4.0.0) and matched with reported ClinVar variations (55).All variants of interest were manually interrogated using the Integrative Genomics Viewer (56).

Structural Variant and CNV Detection

Structural variants (SV) were called with Parliament2 (version 0.1.11; RRID:SCR_019187), utilizing the overlap of the callers lumpy (version 0.2.13; RRID:SCR_003253), CNVnator (version 0.3.3; RRID:SCR_010821), and BreakDancer (version 1.4.3; RRID:SCR_001799); genotyped with SVTyper (version 0.7.0); and merged by SURVIVOR (version 1.0.3; RRID:SCR_022995), using default parameters.

Mutational Signature Analysis

Mutational signature analysis was run on high-confidence variants, using the R package MutationalPatterns (version 3.12.0, RRID:SCR_024247; ref. 57). Variants were converted to categories of mutational spectra for single- and double-base substitutions. Single- and double-base substitution catalogs were obtained from the COSMIC Mutational Signatures database (version 99; RRID:SCR_002260) and compared with sample mutational signatures by calculating the cosine similarity between corresponding count matrices (58).

Lipid Transfer Assays

MSCs and FT190 cells were grown to 70% confluence in a T75 flask and 100% confluence in a single well of a six-well plate, respectively. MSCs were treated with either Lat B or GW4869 overnight. The following day, MSCs were labeled with 2 μmol/L BODIPY FL C12 (Thermo Fisher Scientific; D3822) according to the manufacturer's recommendations. For extracellular vesicle experiments, MSCs were allowed to rest for 1 hour, at which time the conditioned media was centrifuged to remove debris, and media containing EVs were added to CellTrace-labeled FTE cells. FTE cells were alloweed to rest for 4 hours in EV media. For direct contact experiments, MSCs were trypsinized and added to CellTrace-labeled FTE cells and were allowed to rest for 4 hours. Fresh drug was added when inoculating FTE cells. Flow cytometry was used to measure the amount of CellTrace/BODIPY $C12^+$ FTE in both drug- and vehicle-treated groups. Drug efficacy was assessed for Lat B by IF using an F-actin stain, whereas GW4869 efficacy was determined by ultracentrifugation followed by Western blot and probing for mouse anti-CD63 (Abcam, Cat# ab271286, RRID:AB_3675317; 1:1,000).

Experimental Setup

For all *in vitro* experiments, a minimum of $n = 3$ individual repeats were conducted, and where applicable, monoculture controls were used for coculture experiments (i.e., 4-HNE quantification via flow cytometry). For DSP and DNA methylation analysis, data collection and analysis were completed once with varying patient numbers per group as indicated in respective Methods, figure legends, and Results.

Data Availability

The data generated in this study are available within the article and its supplementary data files. Whole-genome sequencing data are publicly available at Mendeley Data, V1, Frisbie, Leonard (2025), "Whole-Genome Sequencing of Initiated Tumors Arising from Pre-malignant Epithelium Coinjected with Mesenchymal Stem Cells in an Intrabursal Murine Model," Mendeley Data, V1, doi: 10.17632/tnx9krc8xz.1. The DNA methylation EPIC array is available at NCBI without restriction (GSE138072). The DSP transcriptomic profile is publicly available at the NCBI Gene Expression Omnibus repository (GSE290451).

Authors' Disclosures

I.P. MacFawn reports grants from the NIH during the conduct of the study as well as personal fees from Galvanize Therapeutics, Inc. outside the submitted work. N. Hempel reports grants from the NIH and Department of Defense (DoD) during the conduct of the study. R. Bao reports other support from the University of Chicago (ClostraBio) outside the submitted work. R. Drapkin reports personal fees from Repare Therapeutics, Light Horse Therapeutics, and ImmunoGen, Inc. outside the submitted work. L.G. Coffman reports grants from the NIH, Tina's Wish, and the Department of Defense during the conduct of the study. No disclosures were reported by the other authors.

Authors' Contributions

G.L. Garcia: Conceptualization, formal analysis, validation, methodology, writing–original draft, writing–review and editing. **T. Orellana:** Formal analysis, investigation, methodology, writing–original draft. **G. Gorecki:** Formal analysis, methodology, writing–original draft. **L. Frisbie:** Formal analysis, investigation, methodology. **R. Baruwal:** Validation, investigation, methodology. **S. Suresh:** Investigation, methodology. **E. Goldfeld:** Investigation, methodology. **I. Beddows:** Conceptualization, formal analysis, investigation, methodology. **I.P. MacFawn:** Validation, investigation, methodology. **A.K. Britt:** Investigation, methodology. **M.M. Hale:** Validation, investigation, methodology. **A.T. Elhaw:** Investigation, methodology. **B.R. Isett:** Conceptualization, software, formal analysis, investigation, methodology. **N. Hempel:** Conceptualization, investigation, methodology, writing–review and editing. **R. Bao:** Conceptualization, formal analysis, methodology. **H. Shen:** Formal analysis, methodology, project administration. **R.J. Buckanovich:** Conceptualization, methodology, writing–review and editing. **T. Finkel:** Conceptualization, resources, methodology. **R. Drapkin:** Conceptualization, resources, methodology. **T.R. Soong:** Conceptualization, formal analysis, validation, methodology. **T.C. Bruno:** Conceptualization, resources, formal analysis, methodology. **H.I. Atiya:** Conceptualization, formal analysis, investigation, methodology, writing–original draft, project administration. **L.G. Coffman:** Conceptualization, resources, formal analysis, supervision, funding acquisition, validation, investigation, methodology, writing–original draft, project administration, writing–review and editing.

Acknowledgments

We would like to thank ProMark and the Pathology Biospecimen Core for tissue acquisition. We would like to thank the UPMC Hillman Cancer Center imaging, flow cytometry, and animal core facilities. We would like to thank the Cancer Bioinformatics Services and the Center for Research Computing. The following sources contributed funding for this work: the Honorable Tina Brozman Foundation (L.G. Coffman and R. Drapkin), DoD Omics Consortium W81XWH-22-1-0852 (L.G. Coffman, R. Bao, and R. Drapkin), DoD Ovarian Cancer Research Program IIRA OC210139 (L.G. Coffman), NIH HCC Ovarian Cancer SPORE P50CA272218-01A1 (L.G. Coffman and R. Bao), NIH U01 AG077923 (L.G. Coffman, R. Bao, and T. Finkel), NIH P50 CA228991 SPORE in ovarian cancer (R. Drapkin), the Miriam and Sheldon G. Adelson Medical Research Foundation (R. Drapkin), NIH R01CA242021 (N. Hempel), UPMC Hillman Cancer Center CCSG award P30CA047904 (B.S. Isett and R. Bao), and NIH S10OD028483 (B.S. Isett and R. Bao).

Note

Supplementary data for this article are available at Cancer Discovery Online (http://cancerdiscovery.aacrjournals.org/).

Received June 3, 2024; revised January 22, 2025; accepted March 6, 2025; posted first March 14, 2025.

REFERENCES

1. Siegel RL, Giaquinto AN, Jemal A. Cancer statistics, 2024. CA Cancer J Clin 2024;74:12–49.
2. Burke W, Barkley J, Barrows E, Brooks R, Gecsi K, Huber-Keener K, et al. Executive summary of the ovarian cancer evidence review conference. Obstet Gynecol 2023;142:179–95.
3. Mei J, Tian H, Huang H-S, Hsu C-F, Liou Y, Wu N, et al. Cellular models of development of ovarian high-grade serous carcinoma: a review of cell of origin and mechanisms of carcinogenesis. Cell Prolif 2021;54:e13029.
4. Reavis HD, Drapkin R. The tubal epigenome–an emerging target for ovarian cancer. Pharmacol Ther 2020;210:107524.
5. Shih I-M, Wang Y, Wang T-L. The origin of ovarian cancer species and precancerous landscape. Am J Pathol 2021;191:26–39.
6. Zhang S, Dolgalev I, Zhang T, Ran H, Levine DA, Neel BG. Both fallopian tube and ovarian surface epithelium are cells-of-origin for high-grade serous ovarian carcinoma. Nat Commun 2019;10:5367.
7. Labidi-Galy SI, Papp E, Hallberg D, Niknafs N, Adleff V, Noe M, et al. High grade serous ovarian carcinomas originate in the fallopian tube. Nat Commun 2017;8:1093.
8. Perets R, Wyant GA, Muto KW, Bijron JG, Poole BB, Chin KT, et al. Transformation of the fallopian tube secretory epithelium leads to high-grade serous ovarian cancer in Brca;Tp53;Pten models. Cancer Cell 2013;24:751–65.
9. Bronder D, Tighe A, Wangsa D, Zong D, Meyer TJ, Wardenaar R, et al. TP53 loss initiates chromosomal instability in fallopian tube epithelial cells. Dis Model Mech 2021;14:dmm049001.
10. Zong Y, Huang J, Sankarasharma D, Morikawa T, Fukayama M, Epstein JI, et al. Stromal epigenetic dysregulation is sufficient to initiate mouse prostate cancer via paracrine Wnt signaling. Proc Natl Acad Sci U S A 2012;109:E3395–404.
11. Wu J, Raz Y, Recouvreux MS, Diniz MA, Lester J, Karlan BY, et al. Focal serous tubal intra-epithelial carcinoma lesions are associated with global changes in the fallopian tube epithelia and stroma. Front Oncol 2022;12:853755.
12. Lochhead P, Chan AT, Nishihara R, Fuchs CS, Beck AH, Giovannucci E, et al. Etiologic field effect: reappraisal of the field effect concept in cancer predisposition and progression. Mod Pathol 2015;28:14–29.
13. Fan H, Atiya HI, Wang Y, Pisanic TR, Wang T-H, Shih I-M, et al. Epigenomic reprogramming toward mesenchymal-epithelial transition in ovarian-cancer-associated mesenchymal stem cells drives metastasis. Cell Rep 2020;33:108473.
14. Frisbie L, Pressimone C, Dyer E, Baruwal R, Garcia G, St Croix C, et al. Carcinoma-associated mesenchymal stem cells promote ovarian cancer heterogeneity and metastasis through mitochondrial transfer. Cell Rep 2024;43:114551.
15. Coffman LG, Choi Y-J, McLean K, Allen BL, di Magliano MP, Buckanovich RJ. Human carcinoma-associated mesenchymal stem cells promote ovarian cancer chemotherapy resistance via a BMP4/HH signaling loop. Oncotarget 2016;7:6916–32.
16. Coffman LG, Pearson AT, Frisbie LG, Freeman Z, Christie E, Bowtell DD, et al. Ovarian carcinoma-associated mesenchymal stem cells arise from tissue-specific normal stroma. Stem Cells 2019;37:257–69.
17. Medeiros F, Muto MG, Lee Y, Elvin JA, Callahan MJ, Feltmate C, et al. The tubal fimbria is a preferred site for early adenocarcinoma in women with familial ovarian cancer syndrome. Am J Surg Pathol 2006;30:230–6.
18. Steele CD, Abbasi A, Islam SMA, Bowes AL, Khandekar A, Haase K, et al. Signatures of copy number alterations in human cancer. Nature 2022;606:984–91.
19. Alexandrov LB, Nik-Zainal S, Wedge DC, Aparicio SAJR, Behjati S, Biankin AV, et al. Signatures of mutational processes in human cancer. Nature 2013;500:415–21.
20. Alexandrov LB, Nik-Zainal S, Wedge DC, Campbell PJ, Stratton MR. Deciphering signatures of mutational processes operative in human cancer. Cell Rep 2013;3:246–59.
21. Cordiano R, Di Gioacchino M, Mangifesta R, Panzera C, Gangemi S, Minciullo PL. Malondialdehyde as a potential oxidative stress marker for allergy-oriented diseases: an update. Molecules 2023;28:5979.
22. Chen J, Zeng L, Xia T, Li S, Yan T, Wu S, et al. Toward a biomarker of oxidative stress: a fluorescent probe for exogenous and endogenous malondialdehyde in living cells. Anal Chem 2015;87:8052–6.
23. Moldogazieva NT, Zavadskiy SP, Astakhov DV, Terentiev AA. Lipid peroxidation: reactive carbonyl species, protein/DNA adducts, and signaling switches in oxidative stress and cancer. Biochem Biophys Res Commun 2023;687:149167.
24. Gronewold TM, Sasse F, Lünsdorf H, Reichenbach H. Effects of rhizopodin and latrunculin B on the morphology and on the actin cytoskeleton of mammalian cells. Cell Tissue Res 1999;295:121–9.
25. Wakatsuki T, Schwab B, Thompson NC, Elson EL. Effects of cytochalasin D and latrunculin B on mechanical properties of cells. J Cell Sci 2001;114:1025–36.
26. Stancu AL. AMPK activation can delay aging. Discoveries (Craiova) 2015;3:e53.
27. Salminen A, Kaarniranta K. AMP-activated protein kinase (AMPK) controls the aging process via an integrated signaling network. Ageing Res Rev 2012;11:230–41.
28. Folkins AK, Jarboe EA, Saleemuddin A, Lee Y, Callahan MJ, Drapkin R, et al. A candidate precursor to pelvic serous cancer (p53 signature) and its prevalence in ovaries and fallopian tubes from women with BRCA mutations. Gynecol Oncol 2008;109:168–73.
29. Levanon K, Ng V, Piao HY, Zhang Y, Chang MC, Roh MH, et al. Primary ex vivo cultures of human fallopian tube epithelium as a model for serous ovarian carcinogenesis. Oncogene 2010;29:1103–13.
30. Karst AM, Drapkin R. Ovarian cancer pathogenesis: a model in evolution. J Oncol 2010;2010:932371.
31. Siegel RL, Miller KD, Wagle NS, Jemal A. Cancer statistics, 2023. CA Cancer J Clin 2023;73:17–48.
32. Sell S. On the stem cell origin of cancer. Am J Pathol 2010;176:2584–494.
33. King SM, Hilliard TS, Wu LY, Jaffe RC, Fazleabas AT, Burdette JE. The impact of ovulation on fallopian tube epithelial cells: evaluating three hypotheses connecting ovulation and serous ovarian cancer. Endocr Relat Cancer 2011;18:627–42.
34. Galhenage P, Zhou Y, Perry E, Loc B, Fietz K, Iyer S, et al. Replication stress and defective checkpoints make fallopian tube epithelial cells putative drivers of high-grade serous ovarian cancer. Cell Rep 2023;42:113144.
35. Huang H-S, Chu S-C, Chu T-Y. Efficient analyses of DNA double-strand breaks and the cell cycle in the secretory epithelial cells of fallopian tube fimbriae. Tzu Chi Med J 2015;27:102–6.
36. Dominici M, Le Blanc K, Mueller I, Slaper-Cortenbach I, Marini F, Krause D, et al. Minimal criteria for defining multipotent mesenchymal stromal cells. The International Society for Cellular Therapy position statement. Cytotherapy 2006;8:315–7.
37. Karst AM, Drapkin R. Primary culture and immortalization of human fallopian tube secretory epithelial cells. Nat Protoc 2012;7:1755–64.
38. Mootha VK, Lindgren CM, Eriksson K-F, Subramanian A, Sihag S, Lehar J, et al. PGC-1alpha-responsive genes involved in oxidative phosphorylation are coordinately downregulated in human diabetes. Nat Genet 2003;34:267–73.
39. Subramanian A, Tamayo P, Mootha VK, Mukherjee S, Ebert BL, Gillette MA, et al. Gene set enrichment analysis: a knowledge-based approach for interpreting genome-wide expression profiles. Proc Natl Acad Sci U S A 2005;102:15545–50.
40. Zhou W, Triche TJ, Laird PW, Shen H. SeSAMe: reducing artifactual detection of DNA methylation by Infinium BeadChips in genomic deletions. Nucleic Acids Res 2018;46:e123.

41. Healy J, McInnes L. Uniform manifold approximation and projection. Nat Rev Methods Primers 2024;4:82.
42. Barbolina MV, Adley BP, Shea LD, Stack MS. Wilms tumor gene protein 1 is associated with ovarian cancer metastasis and modulates cell invasion. Cancer 2008;112:1632–41.
43. Hylander B, Repasky E, Shrikant P, Intengan M, Beck A, Driscoll D, et al. Expression of Wilms tumor gene (WT1) in epithelial ovarian cancer. Gynecol Oncol 2006;101:12–7.
44. Taube ET, Denkert C, Sehouli J, Kunze CA, Dietel M, Braicu I, et al. Wilms tumor protein 1 (WT1)–not only a diagnostic but also a prognostic marker in high-grade serous ovarian carcinoma. Gynecol Oncol 2016;140:494–502.
45. Yamamoto S, Tsuda H, Kita T, Maekawa K, Fujii K, Kudoh K, et al. Clinicopathological significance of WT1 expression in ovarian cancer: a possible accelerator of tumor progression in serous adenocarcinoma. Virchows Arch 2007;451:27–35.
46. Han Y, Song C, Zhang T, Zhou Q, Zhang X, Wang J, et al. Wilms' tumor 1 (WT1) promotes ovarian cancer progression by regulating E-cadherin and ERK1/2 signaling. Cell Cycle 2020;19:2662–75.
47. Atiya HI, Orellana TJ, Wield A, Frisbie L, Coffman LG. An orthotopic mouse model of ovarian cancer using human stroma to promote metastasis. J Vis Exp 2021;169:e62382.
48. Agorku DJ, Tomiuk S, Klingner K, Wild S, Rüberg S, Zatrieb L, et al. Depletion of mouse cells from human tumor xenografts significantly improves downstream analysis of target cells. J Vis Exp 2016;113:54259.
49. Tarasov A, Vilella AJ, Cuppen E, Nijman IJ, Prins P. Sambamba: fast processing of NGS alignment formats. Bioinformatics 2015;31:2032–4.
50. Li H, Handsaker B, Wysoker A, Fennell T, Ruan J, Homer N, et al. The sequence alignment/map format and SAMtools. Bioinformatics 2009;25:2078–9.
51. DePristo MA, Banks E, Poplin R, Garimella KV, Maguire JR, Hartl C, et al. A framework for variation discovery and genotyping using next-generation DNA sequencing data. Nat Genet 2011;43:491–8.
52. Van der Auwera GA, Carneiro MO, Hartl C, Poplin R, Del Angel G, Levy-Moonshine A, et al. From FastQ data to high confidence variant calls: the Genome Analysis Toolkit best practices pipeline. Curr Protoc Bioinformatics 2013;43:11.10.1–11.10.33.
53. Kim S, Scheffler K, Halpern AL, Bekritsky MA, Noh E, Källberg M, et al. Strelka2: fast and accurate calling of germline and somatic variants. Nat Methods 2018;15:591–4.
54. Tan A, Abecasis GR, Kang HM. Unified representation of genetic variants. Bioinformatics 2015;31:2202–4.
55. Landrum MJ, Lee JM, Benson M, Brown GR, Chao C, Chitipiralla S, et al. ClinVar: improving access to variant interpretations and supporting evidence. Nucleic Acids Res 2018;46:D1062–7.
56. Robinson JT, Thorvaldsdóttir H, Winckler W, Guttman M, Lander ES, Getz G, et al. Integrative genomics viewer. Nat Biotechnol 2011;29:24–6.
57. Blokzijl F, Janssen R, van Boxtel R, Cuppen E. MutationalPatterns: comprehensive genome-wide analysis of mutational processes. Genome Med 2018;10:33.
58. Tate JG, Bamford S, Jubb HC, Sondka Z, Beare DM, Bindal N, et al. COSMIC: the catalogue of somatic mutations in cancer. Nucleic Acids Res 2019;47:D941–7.